Remote Sensing of Environment 317 (2025) 114521

Contents lists available at ScienceDirect

Remote Sensing of Environment

journal homepage: www.elsevier.com/locate/rse

# Comparing methods for solar-induced fluorescence efficiency estimation using radiative transfer modelling and airborne diurnal measurements of barley crops

Juliane Bendig [a,b,c,*], Zbyněk Malenovský [a,d], Bastian Siegmann [c], Julie Krämer [c], Uwe Rascher [c]

[a] School of Geography, Planning, and Spatial Sciences, College of Sciences Engineering and Technology, University of Tasmania, Private Bag 76, 7001 Hobart, Australia
[b] Centre d'Etudes Spatiales de la Biosphère, 18 avenue Edouard Belin BPI 2801, 31401 Toulouse Cedex 9, France
[c] Institute for Bio- and Geosciences, IBG-2: Plant Sciences, Forschungszentrum Jülich GmbH, Wilhelm-Johnen-Straße, 52428 Jülich, Germany
[d] Remote Sensing Research Group, Department of Geography, University of Bonn, Meckenheimer Allee 166, 53115 Bonn, Germany

ARTICLE INFO

Edited by Jing M. Chen

*Keywords:*
Chlorophyll fluorescence efficiency
SIF escape probability
FCVI
NIRv
Discrete anisotropic radiative transfer
Drone
HyPlant

ABSTRACT

Ability of remotely sensed solar-induced chlorophyll fluorescence (SIF) to serve as a vegetation productivity and stress indicator is impaired by confounding factors, such as varying crop-specific canopy structure, changing solar illumination angles, and SIF-soil optical interactions. This study investigates two normalisation approaches correcting diurnal top-of-canopy SIF observations retrieved from the $O_2$-A absorption feature at 760 nm ($F_{760}$ hereafter) of summer barley crops for these confounding effects. Nadir SIF data was acquired over nine breeding experimental plots simultaneously by an airborne imaging spectrometer (HyPlant) and a drone-based high-performance point spectrometer (AirSIF). Ancillary measurements, including leaf pigment contents retrieved from drone hyperspectral imagery, destructively sampled leaf area index (LAI), and leaf water and dry matter contents, were used to test the two normalisation methods that are based on: i) the fluorescence correction vegetation index (FCVI), and ii) three versions of the near-infrared reflectance of vegetation ($NIR_V$). Modelling in the discrete anisotropic radiative transfer (DART) model revealed close matches for NIRv-based approaches when corrected canopy SIF was compared to simulated total chlorophyll fluorescence emitted by leaves ($R^2 = 0.99$). Normalisation with the FCVI also performed acceptably ($R^2 = 0.93$), however, it was sensitive to variations in LAI when compared to leaf emitted chlorophyll fluorescence efficiency. Based on the results modelled in DART, the NIRvH1 normalisation was found to have a superior performance over the other NIRv variations and the FCVI normalisation. Comparison of the SIF escape fractions suggests that the escape fraction estimated with NIRvH1 matched escape fraction extracted from DART more closely. When applied to the experimental drone and airborne nadir canopy SIF data, the agreement between NIRvH1 and FCVI produced chlorophyll fluorescence efficiency was very high ($R^2 = 0.93$). Nevertheless, NIRvH1 showed higher uncertainties for areas with low vegetation cover indicating an unaccounted contribution of SIF-soil interactions. The diurnal courses of chlorophyll fluorescence efficiency for both approaches differed not significantly from simple normalisation by incoming and apparent photosynthetically active radiation. In conclusion, SIF normalisation with NIRvH1 more accurately compensates the effects of canopy structure on top of canopy far red SIF, but when applied to top of canopy in-situ data of spring barley, the effects of NIRvH1 and FCVI on the diurnal course of SIF had a similar influence.

## 1. Introduction

Chlorophyll fluorescence (ChlF) is gaining increased attention as a tool for vegetation monitoring because it enables measuring actual photosynthesis of plants (Mohammed et al., 2019). ChlF is a weak optical signal emitted by plants during photosynthesis, representing energy that could not be used in photochemical energy transport or non-photochemical energy dissipation. Thus, the intensity of the

* Corresponding author at: Institute for Bio- and Geosciences, IBG-2: Plant Sciences, Forschungszentrum Jülich GmbH, Wilhelm-Johnen-Straße, 52428 Jülich, Germany.
*E-mail addresses:* j.bendig@fz-juelich.de (J. Bendig), b.siegmann@fz-juelich.de (B. Siegmann), ju.kraemer@fz-juelich.de (J. Krämer), u.rascher@fz-juelich.de (U. Rascher).

https://doi.org/10.1016/j.rse.2024.114521
Received 2 February 2024; Received in revised form 22 October 2024; Accepted 14 November 2024
Available online 26 November 2024

fluorescence signal, combined with additional information on absorbed light energy distribution, can be a proxy for the functional status of actual photosynthesis. Measuring the quantity and spatio-temporal dynamics of ChlF allows us to assess and better understand the dynamic interaction of plant photosynthesis and its environmental factors. Thus remote sensing of ChlF is widely used in plant sciences and the recently increasing capabilities to measure solar-induced fluorescence (SIF) also from airborne and satellite platforms have triggered a wide variety of studies, which e.g. have shown that SIF has the potential to improve modelling of gross primary productivity (GPP) (Wieneke et al., 2016), detect early signs of vegetation stress (Xu et al., 2021), and guide management practices in agriculture (Zarco-Tejada et al., 2016).

In remote sensing, the factors interfering and consequently attenuating the ChlF signal emitted and scaled from leaves to canopy level are of particular interest. The signal scattering and re-absorption by canopy structures and soil beneath them depend on spatial, in case of agricultural crops mainly vertical, canopy architectural heterogeneity (e.g., Regaieg et al., 2021). Additionally, effects of optical measurement geometry (i.e., an angular setup of the sun-target-sensor system) have been identified as factors decoupling the photosynthesis - SIF relationship (Hao et al., 2021; Porcar-Castell et al., 2021; Zhang et al., 2022).

Airborne SIF measurements can be acquired from airplanes or remotely piloted multirotor drones, typically producing SIF canopy observations with a spatial resolution of <2 m. Observations of the airborne imaging spectrometer HyPlant (Rascher et al., 2015) are classical airborne imaging spectroscopy surveys coupled with a well characterised image data processing chain producing images with an absolute positional accuracy of ±2 pixel (Siegmann et al., 2019). Drone-based observations of SIF are less established and associated with specific operational challenges (Bendig et al., 2021). At present, only a low number of drones equipped with specific sensors exist, which can measure SIF in radiance units. The dataset used in this study is one of the few presenting repeated measurements throughout a day (Chang et al., 2020; Wang et al., 2021), and only the second study where drone data were recorded simultaneously with an airborne reference instrument (HyPlant) (Wang et al., 2022). All current SIF drone systems consist of multirotor remotely piloted airborne systems (RPAS) equipped with light-weight (<1 kg) non-imaging spectroradiometers (Vargas et al., 2020). Mounting a spectroradiometer on an RPAS requires a rigorous and reliable compensation for sensor tilting during flight, which brings challenges in spectroradiometer system design, as for example accuracy of downwelling irradiance measurements acquired with a cosine receptor. For applications with required absolute geometric accuracy of the observations below 2 m, the accuracy of drone navigation and positioning is as crucial as a characterization of the projected spectroradiometer field of view (i.e., footprint) on the ground during flight (Gautam et al., 2020). The latter is the prerequisite for a full comparability with measurements of the same canopy locations collected by other SIF-measuring sensors (Bendig et al., 2021).

In addition to uncertainties arising from the sensor design and related measuring equipment, the low energy level of the SIF signal, equal to 1–5 % of reflected radiance, and the retrieval techniques, using atmospheric oxygen absorption features, make comparisons of SIF acquired by different sensors at varying scales particularly challenging. Furthermore, top-of-canopy (TOC) observations are not comparable with SIF measurements of single leaves due to the optical interactions (i.e., scattering and absorption) of the SIF signal and interactions of the incident photosynthetically active radiation (PAR) with canopy elements and soil organised in specific three-dimensional (3D) architectures (Malenovský et al., 2021). Besides the fact the quantification of absorbed PAR (APAR) by individual plants depends on the actual canopy structure, Fournier et al. (2012) and Yang et al. (2019) showed that structural parameters such as LAI and leaf angles, as well as biochemical traits such as leaf chlorophyll *a*nd dry matter content, influence TOC SIF observations and that canopy reflectance plays an important role in disentangling these effects. In an attempt to eliminate impacts associated with scaling ChlF from leaf to canopy scale, both APAR and PAR have been used to normalise TOC SIF measurements as so-called SIF yield (e.g. Biriukova et al., 2020; Zhang et al., 2020). Guanter et al. (2014) approached the canopy structure confounding problem by defining the fluorescence escape fraction ($f_{esc}$) as the fraction of leaf SIF that is escaping from the top of the canopy. Yang and van der Tol (2018) explored the directional scattering of $F_{760}$ and found that it can be expressed as a simple function of canopy APAR interception, TOC reflectance, and leaf albedo. In a later study of Liu et al. (2019), the TOC SIF normalisation was attempted with a machine-learning random forest approach. Since the concept of SIF normalisation with APAR was found to be promising, it was further developed by Zeng et al. (2019) within a normalisation of SIF satellite observations with the near-infrared reflectance of vegetation (NIRv) index, calculated as NIR canopy reflectance multiplied by the normalised difference vegetation index (NDVI). Here, NIRv divided by the fraction of canopy APAR (fAPAR) is used as a proxy of the fraction of photons that escape from the canopy in near-infrared wavelengths ($f_{escN}$). Following a similar concept, based on the spectral invariant theory of Knyazikhin et al. (2013), Yang et al. (2020) developed an approach to normalise $F_{760}$. They suggested fluorescence correction vegetation index (FCVI), which is built on a stronger mechanistic basis than the earlier semi-empirical methods. Like the concept of SIF yield, normalisation of canopy $F_{760}$ with FCVI results in the $F_{760}$ efficiency, which represents a proxy of total SIF at the leaf level emitted in nadir direction. Zeng et al. (2021) improved the NIRv concept by estimating the true NIR reflectance from remotely sensed hyperspectral observations and introduced two new variants of the index, i.e., NIRvH1 and NIRvH2.

The scientific motivation of this study is to test the capability of the FCVI and NIRv-based standardisation approaches (NIRvH1/H2 hereafter) to separate structural and physiological parts of TOC $F_{760}$, when applied on data acquired at a range of solar radiance incidence angles covering multiple diurnal instances during one of the European Space Agency (ESA) FLEXSense 2018 campaign days. We aim to investigate correspondence and difference of $F_{760}$ efficiency with the FCVI and NIRvH1/H2 standardisation approaches computed from drone and aircraft observations acquired at comparable spatial scales (~1 m pixel/footprint size) over a barley breeding experiment in Western Germany on 29 June 2018. As the data was recorded at different solar illumination angles and for experimental plots with a spatially heterogeneous canopy architecture, the SIF radiance observations had to be standardised to SIF canopy efficiencies to allow for direct comparison of the physiologically based SIF information among trial plots of four winter barley varieties. The first objective was to test the performance and limitations of the two canopy SIF efficiency standardisation methods, i.e.: i) FCVI, and ii) NIRv as well as NIRvH1/H2, in a virtual environment of the three-dimensional (3D) discrete anisotropic radiative transfer (DART) model (Gastellu-Etchegorry et al., 2017). The second objective was to apply both standardisation methods to SIF observations acquired during the same day with two technically different drone and aerial sensor platforms, and to evaluate their advantages and shortcomings for their potential use in calibration/validation activities of, for instance, the future ESA FLEX mission designed to provide global space-borne SIF observations.

## 2. Materials and methods

### 2.1. Study site

The study site is located at Campus Klein-Altendorf agricultural research station near Bonn in Western Germany (50°37′25.30″N, 6°59′14.06″E, altitude 225 m a.s.l.). The spring barley (*Hordeum vulgare*) experiment consisted of 35 plots with 10 varieties, each of which with different structural and functional traits, planted in a randomised block design with a sowing density of 330 seeds/$m^2$. Each experimental plot had a size of 3 by 6 m. Destructive and non-destructive sampling of nine

plots of four barley varieties was conducted on 29 June 2018, 82 days after sowing. The crop phenology status was either late fruit development or early ripening stage, corresponding to the classes 77–85 on the Biologische Bundesanstalt, Bundessortenamt and CHemical industry (BBCH) crop development scale. Some plots in the early ripening stage were partially or completely lodged. The early ripening can be attributed to the 2018 European heat wave, which was characterised by an unusually warm spring followed by hot and dry summer with an average temperature of 3.6 K above the long term mean, the highest positive anomaly since 1881 (Imbery et al., 2018).

### 2.2. Dataset

#### 2.2.1. Ground sampling of experimental plots

To obtain reference information about the growing barley plots at the time of the experiment, one representative plant per plot was removed for laboratory analysis of leaf area index, dry matter, and water content (Table 1). The area of freshly harvested leaves was measured using an Li—3200C Leaf Area Meter (LI-COR, USA). The samples were subsequently stored at 65 °C in a drying cabinet until they were completely dried to determine their dry weight and water content. Known sowing density (the distance between single plants) and the row spacing at each sampling location allowed for upscaling the measurements of leaf area index (LAI) and dry weight determined for individual plants to one square metre of each experimental plot.

#### 2.2.2. Drone-based data

Four flights with the drone-based spectroradiometer payload "AirSIF" were conducted on 29 June 2018 at 12:00, 14:00, 15:30, and 17:00 local time (solar noon was 13:35) under clear sky conditions. AirSIF is based on a single spectroradiometer with optical shutters and a *conical-hemispherical* combination of optical fibres. The AirSIF QE Pro spectroradiometer (Ocean Insight Inc., USA), having a spectral sampling interval of 0.37 nm, full width at half maximum (FWHM) of 0.8 nm, and a spectral range from 500 to 870 nm, is integrated on a DJI Matrice 600 Pro (SZ DJI Technology Co., Ltd., China) drone platform (Bendig et al., 2019). Downwelling irradiance is measured with a cosine receptor foreoptic and the upwelling radiance channel field of view (FOV) is restricted by a Gershun tube to 8° (Ocean Insight, Inc. USA). Furthermore, the upwelling radiance measuring channel was, together with an inertial measurement unit (IMU) combined with a global navigation satellite system (GNSS), mounted on an automatically stabilising gimbal. To maximise the number of vegetation target measurements, upwelling radiance was measured every ~1 s, while downwelling irradiance only every 15 s. A boom with a dual GNSS antenna was mounted on top of the drone airframe, to enable a real time kinematic (RTK) position correction of the spectroradiometer observations during data post processing. A detailed technical description of the AirSIF hardware system can be found in Gautam et al. (2020). Since IMU measurements and spectroradiometer observations are interlinked through time stamps, the spectroradiometer's instantaneous FOV is determined after correcting IMU positions for lever arm and boresight offsets by applying a ray tracing algorithm (Gautam et al., 2020, 2019). The algorithm subsequently projects the FOV onto a Digital Surface Model (DSM), considering the drone height above ground (8 m), flying speed (2 $m \cdot s^{-1}$), and spectroradiometer integration time (700–900 ms). The output of the ray tracing projection is a polygon shapefile with the instantaneous FOV ground footprints of the spectroradiometer that can be used in further spatial analysis (see Fig. 8). To record as many pure vegetation spectra within the targeted sample plots as possible, AirSIF was flown to the centre of each plot and hovered above for 20 s while continuously acquiring spectral measurements.

Besides SIF measurements, overlapping RGB images (photographs) were acquired with a Phantom 4 Pro drone (SZ DJI Technology Co., Ltd., China) equipped with a built-in RGB digital camera. The orthophoto and DSM of the study site were derived from overlapping RGB imagery with a ground sampling distance (GSD) of 0.02 m by applying photogrammetric methods using Agisoft Metashape software (Version 1.5.5, Agisoft LLC, Russia) (Mancini et al., 2013). Absolute geometric accuracy of 0.06 m was achieved when using eight ground control points, measured with an RTK GNSS device (HiPer Pro, Topcon, Japan).

On 2 July 2018, the Matrice 600 Pro drone was equipped with the visible near infrared (VNIR) imaging spectroradiometer Micro-Hyperspec (Headwall Photonics Inc., USA), acquiring hyperspectral images with a 400 to 1000 nm spectral range, spectral sampling interval of 3.7 nm, and mean FWHM of 5.05 nm. The payload is similar to the system described in Lucieer et al. (2014), but it was upgraded with a stabilising gimbal. The study site was overflown at 13:00 local time at 15 m flying height, resulting in five hyperspectral flight lines with 60 % side overlap. Raw image data were processed to at-sensor radiance with GSD of 0.04 m. Flight lines were geo-rectified with the Parametric Geocoding & Orthorectification for Airborne Optical Scanner Data (PARGE) software (ReSe Applications GmbH, Switzerland). Mosaicking of the flight lines was performed in the ENVI image analysis software (Harris Geospatial Solutions, Inc., USA). The hyperspectral TOC radiance orthomosaic was then used to estimate mean leaf chlorophyll $a + b$ content per investigated experimental plot (see section 2.3.3.1).

#### 2.2.3. Aircraft data

The HyPlant sensor is a hyperspectral imaging system for airborne data acquisition developed by the Forschungszentrum Jülich (Germany) in cooperation with the company Specim Ltd. (Finland). It consists of two sensor heads. First, the DUAL module consists of two line-imaging push-broom hyperspectral sensors utilising a common fore objective lens and providing contiguous spectral information from 370 to 2500 nm with a FWHM of 3.65 nm in the VNIR and 10.55 nm in the short

**Table 1**
Overview of barley plot parameters derived from destructive laboratory analysis of sampled individual plants collected on 29 June 2018. Leaf chlorophyll $a + b$ content was retrieved from a hyperspectral orthomosaic by inversion of the PROSAIL radiative transfer model (see sections 2.2.2 and 2.3.3.1). BBCH stands for Biologische Bundesanstalt, Bundessortenamt and CHemical industry crop development scale, and LAI stands for leaf area index.

| Plot ID | Variety | BBCH crop development stage | LAI [$m^{-2} \cdot m^{-2}$] | Dry matter content ($C_{dm}$) [$g \cdot cm^{-2}$] | Water content ($C_w$) [cm] | Chlorophyll $a + b$ content ($C_{ab}$) [$\mu g \cdot cm^{-2}$] |
|---|---|---|---|---|---|---|
| 200 | HOR21770 | 83 | 9.53 | 0.0044 | 0.0126 | 43.565 |
| 217 | HOR21770 | 83 | 8.05 | 0.0041 | 0.0110 | 40.271 |
| 228 | HOR21770 | 83 | 6.32 | 0.0044 | 0.0081 | 44.835 |
| 205 | HOR11300 | 77 | 8.00 | 0.0034 | 0.0434 | 32.179 |
| 212 | HOR3939 | 85 | 4.01 | 0.0044 | 0.0041 | 36.469 |
| 222 | HOR3939 | 83 | 1.80 | 0.0009 | 0.0023 | 38.562 |
| 203 | HOR9707 | 83 | 3.74* | N/A | N/A | 39.168 |
| 215 | HOR9707 | 83 | 3.74* | N/A | N/A | 39.939 |
| 233 | HOR9707 | 83 | 3.74 | 0.0034 | 0.0038 | 40.572 |

* Due to missing laboratory measurements, LAI was estimated from plot 233 having the same crop variety and comparable mean normalised difference vegetation index (NDVI) of 0.36 (plot 203), 0.36 (plot 215), and 0.41 (plot 233), respectively.

wavelength infrared (SWIR) spectral range. Second, SIF is measured with a separate FLUO push-broom sensor, which records data in the range between 670 and 780 nm with a distinctly finer spectral resolution (FWHM = 0.28 nm). The FLUO spectral characteristics enable retrieving SIF inside the $O_2$-A and $O_2$—B absorption features located at 760 and 687 nm, respectively. A detailed description of the HyPlant sensor system can be found in Siegmann et al. (2019) and Rascher et al. (2015).

The HyPlant sensor system was installed aboard a Cessna 208B Grand Caravan aircraft operated by the Global Change Research Institute (Czech Academy of Sciences, Czech Republic). The study site was overflown six times on 29 June 2018 at two different flight altitudes: i) 350 m (12:42 and 14:54) and ii) 680 m above ground level (11:15, 12:29, 14:40, and 15:54), leading to GSDs of 0.5 by 1 m and 1 by 1 m, respectively.

The raw data acquired by both sensor modules were processed to final image products using the standardised HyPlant processing chain. First, the CaliGeoPro software (Specim Ltd., Finland) was used to radiometrically correct HyPlant DUAL and FLUO data to produce at-sensor radiance and subsequently SIF was retrieved from FLUO radiance data (see section 2.3.1.3). To obtain top of canopy (TOC) radiance and reflectance from the DUAL data atmospheric correction was conducted in the ATCOR-4 software (ReSe Applications GmbH, Switzerland). Exact locations and orientations measured with GNSS and IMU systems during HyPlant DUAL and FLUO data acquisitions were used to facilitate geometric corrections of the flight lines. An extensive description of the HyPlant processing chain used in this study can be found in Siegmann et al. (2019).

## 2.3. Data processing

### 2.3.1. Field and airborne vegetation canopy properties

*2.3.1.1. Estimation of crop leaf angle distribution.* Due to the varying canopy height, induced by crop lodging, a strong influence of leaf angle distribution on traits retrieved from remote sensing data was assumed. Therefore, we quantified the amount of non-lodging and lodging barley plants in each sampled plot using the slope of the crop DSM (Fig. 1). A slope analysis was conducted in ArcGIS Desktop (v10, Esri Inc., USA), due to its previously shown suitability for detecting damaged crops (Garcia Millan et al., 2020). As a first step, a digital terrain model, constructed by applying the ArcGIS function "trend", was subtracted from the DSM to derive a crop surface model (CSM). Next, the slope of the CSM was calculated, and a slope threshold of 35°, chosen based on the Otsu-Method for histogram analysis (Otsu, 1979), was applied to detect edges of lodging areas. This process resulted in a binary raster mask of the classes "edge" and "other", which was converted to polygons while removing very small areas (<0.3 $m^2$). The class "other" was then split into "non-lodging" and "lodging" parts based on the actual CSM height differences with the ArcGIS "rescale by function" tool. The leaf angle distribution (LAD) of the "lodging" class was assumed as planophile and of the "non-lodging" class as spherical. This classification enabled a calculation of the percentage of planophile and spherical LAD in each plot, which was consequently used for modelling of fAPAR in DART simulations (see section 2.3.3.2).

*2.3.1.2. Photosynthetically active radiation.* PAR present at the time of measurement is a quantity often used for normalising SIF. PAR was estimated from downwelling irradiance of the AirSIF system as the average of irradiance measurements taken during each flight (Fig. 1). To cover the PAR spectral range of 400–700 nm, AirSIF downwelling irradiance (500–700 nm) had to be extrapolated towards 400 nm. A linear model was fitted to the measured irradiance between 500 and 520 nm and applied to estimate the missing values between 400 and 500 nm. Finally, spectrally resolved measurements in $W{\cdot}m^{-2}{\cdot}nm^{-1}{\cdot}sr^{-1}$ were integrated to PAR in $W{\cdot}m^{-2}$. The diurnal course of PAR was reconstructed by fitting a polynomial function and PAR values for HyPlant flights, temporally slightly offset from AirSIF flights, were predicted using the best statistical fit (see Fig. 2).

*2.3.1.3. SIF retrieval.* Spectra collected with the AirSIF instrument were

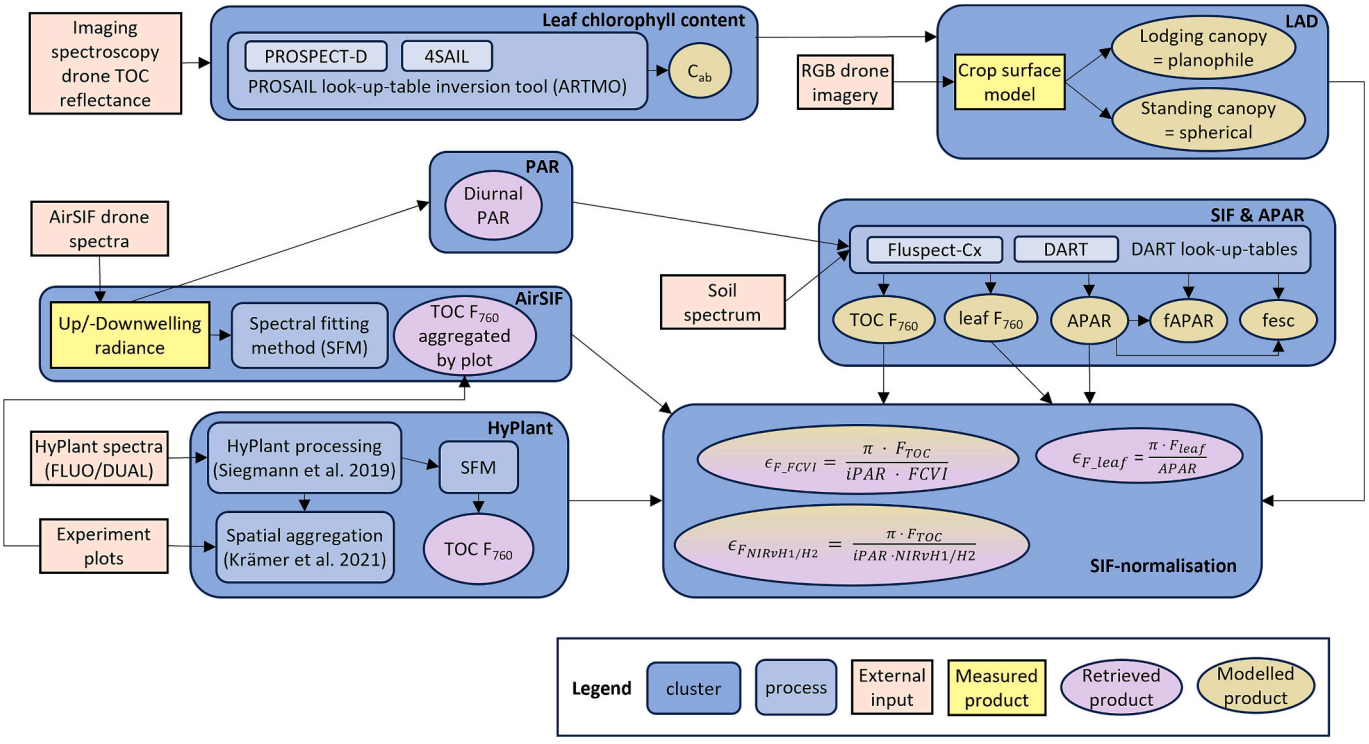


**Fig. 1.** Overview of the data processing workflow. PROSPECT-D, 4SAIl, Fluspect-Cx, DART are radiative transfer models, TOC is top of canopy, PAR is photosynthetically active radiation, APAR and fAPAR are apparent PAR and fraction of APAR respectively.

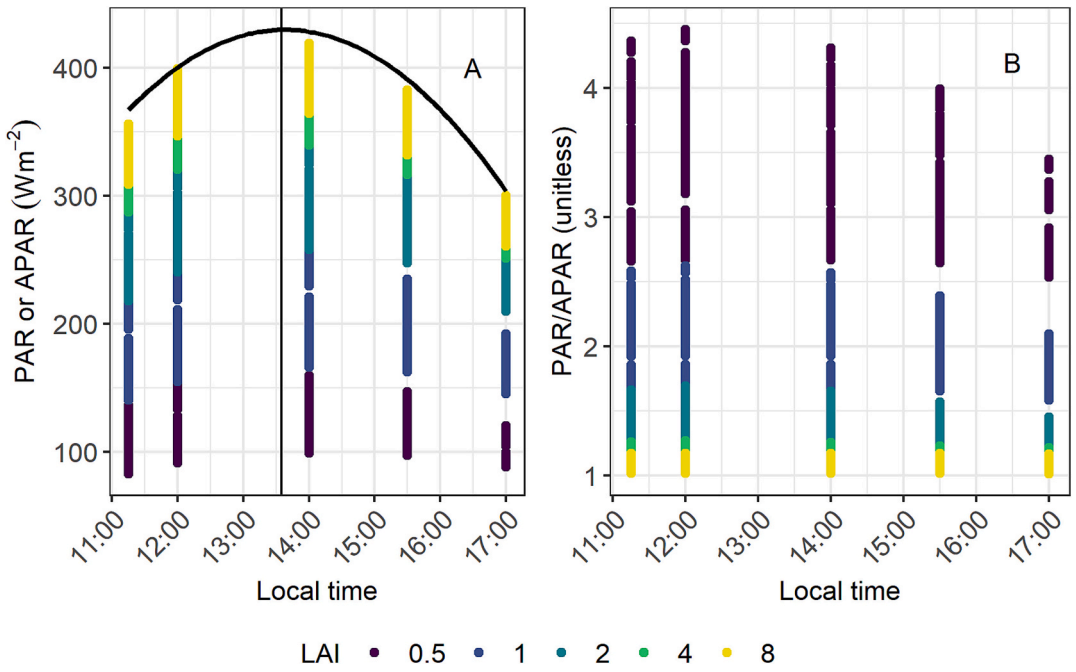


**Fig. 2.** (A) DART-simulated PAR (W.m$^{-2}$, black line, interpolated using 2nd order polynomial), black vertical line ~ solar noon, and APAR (W·m$^{-2}$, coloured by LAI), between 11:15 (38.6° SZA) and 17:00 CEST (47.87° SZA) on 29 June 2018. (B) The same data visualised as the ratio of PAR to APAR. Input values for the DART simulations are listed in Table 3.

converted from intensity digital numbers to physical at-sensor radiance units by applying laboratory measured radiometric calibration coefficients. Each upwelling radiance measurement was coupled to the downwelling irradiance measurement collected at the closest time. $F_{760}$ was retrieved by applying the spectral fitting method (SFM) (Meroni et al., 2010; Meroni and Colombo, 2006) implemented in the SpecFit Matlab algorithm (Cogliati et al., 2015).

To retrieve $F_{760}$ from HyPlant FLUO data, an airborne-based implementation of the SFM was applied. The SFM was originally introduced by Cogliati et al. (2015) and later improved for more robust characterization of atmospheric interferences. It is based on a combined surface-atmospheric radiative transfer modelling, which is applied to generate at-sensor radiance spectra around the $O_2$-A absorption band. The MODTRAN5 model (Berk et al., 2005) is used to simulate transmittances, path radiance, and spherical albedo to represent atmospheric absorption and scattering effects (details in Rascher et al., 2022; Siegmann et al., 2019). Subsequently, mathematical functions, i.e., polynomial, and Gaussian-like functions, are employed to model SIF and reflectance spectra. The actual retrieved $F_{760}$ corresponds to the one with the best fit between simulated and measured at-sensor radiances.

*2.3.1.4. AirSIF drone footprint selection.* With the aim to use high-quality and statistically robust spectra collected within the experimental plot boundaries, each AirSIF spectroradiometer footprint had to be screened and examined for sufficient spectral information of the barley canopy. In a first step, footprints having their centroid within a sampled plot were preselected. In a next step, the area of each footprint lying within the plot boundaries was calculated and footprints with less than 50 % area inside the plot boundaries were removed (Fig. 6). This threshold was chosen to keep enough footprints per flight, and to satisfy the assumption that the majority of the spectroradiometer signal originates from the footprint centre. The spectral response within the FOV of the spectroradiometer is assumed to have a three-dimensional Gaussian spectral shape that rapidly declines towards the footprint edges (Mac Arthur et al., 2012). The spatial analysis was conducted in ArcGIS Desktop (v10, Esri Inc., USA).

*2.3.1.5. HyPlant airborne data pixel aggregation.* To extract SIF information for each experimental plot from HyPlant SIF data, we applied a spatial aggregation approach developed by Krämer et al. (2021). We first masked out outlier pixels in geometrically corrected at-sensor radiance data of the FLUO module according to a robust outlier detection scheme. Here, we chose a modified version of the widely used Hampel identifier, which was found to be highly resistant to outlier values (Hampel, 1974). The modification consisted of substituting the MAD scale estimator by the mean of absolute deviations for the samples' median to avoid implosion effects (Krämer et al., 2021). Next, we produced a shapefile containing geospatial vector data of single experimental plots including a negative buffer of 0.3 m reducing the border effect, as shown in Fig. 6. Based on the geospatial vector data, we aggregated radiance of every experimental plot by applying a weighted mean function, where weights corresponded to the fractional canopy cover of pixels within the buffered plot outlines. In a last step, SIF values for individual barley plots were extracted from the aggregated radiance spectra by applying the SFM retrieval, as described in section 2.3.1.3 (see also Fig. 1). More details on the aggregation SIF retrieval method can be found in Krämer et al. (2021).

### 2.3.2. SIF normalisation

$F_{760}$ was normalised to the fluorescence efficiency factor as suggested by Yang et al. (2020). The method design starts with the factors influencing TOC SIF, expressed in the light use efficiency model equation for GPP estimation as:

$$F_{TOC} = iPAR \bullet fAPAR_{green} \bullet \varepsilon_F \bullet f_{esc}, \quad (1)$$

where $F_{TOC}$ is $F_{760}$ measured at TOC level, iPAR is the TOC incoming PAR, $fAPAR_{green}$ is the fraction of absorbed PAR by green canopy foliage, $\varepsilon_F$ is SIF efficiency, defined as the apparent $\varepsilon_F$ at the whole leaf level in nadir direction, and $f_{esc}$ is the fluorescence escape fraction. The SIF efficiency factor aims at minimising impact of physical interactions of PAR as well as $F_{760}$ with structural elements inside the canopy, resulting in photon scattering and absorption. The effect of vegetation canopy structure on these two processes was proposed to be characterised by the fluorescence correction vegetation index (FCVI):

$$FCVI = R_{NIR} - R_{\underline{VIS}}, \quad (2)$$

where $R_{NIR}$ is the directional reflectance at the NIR plateau, in this study 767–772 nm, and $R_{\underline{VIS}}$ is the broadband visible reflectance between 400 and 700 nm. Consequently, the FCVI-based fluorescence efficiency ($\epsilon_{F\_FCVI}$) was computed as:

$$\epsilon_{F\_FCVI} = \frac{\pi \cdot F_{TOC}}{iPAR \cdot FCVI}, \quad (3)$$

where the units of $F_{TOC}$ and iPAR are $mW \cdot m^{-2} \cdot nm^{-1} \cdot sr^{-1}$ and $mW \cdot m^{-2}$, respectively, producing $\epsilon_{F\_FCVI}$ in $nm^{-1}$.

The second tested approach is standardisation with NIRv and its extensions NIRvH1 and NIRvH2. NIRvH1 uses a single vector decomposition to estimate the soil single scattering contribution and a logistic function to estimate the bi-directional reflectance factor of vegetation at the red edge, i.e., wavelengths at 675–800 nm (Zeng et al., 2021). NIRvH2 is its simpler version, where a soil reflectance spectrum within red edge is assumed to be linear. NIRv-based fluorescence efficiency ($\epsilon_{F_{NIRvH1/H2}}$) was computed as:

$$\epsilon_{F_{NIRvH1/H2}} = \frac{\pi \cdot F_{TOC}}{iPAR \cdot NIRvH1/H2}, \quad (4)$$

A shortcoming of SIF normalisation methods using iPAR is the assumption that the amount of PAR absorbed by the canopy (APAR) can be approximated by the actual iPAR quantity. This assumption, however, neglects influence originating from solar illumination angles in combination with the canopy architecture and soil background that, in turn, cause decoupling of iPAR and APAR. To test and compare performance of this approach, we modelled canopy APAR and SIF for our experimental barley plots in the DART model (Gastellu-Etchegorry et al., 2017), analysed the 3D radiative budget of iPAR per-canopy, APAR, and $F_{760}$, i.e., a combined leaf SIF emission from photosystem I and II (PSI and PSII), modelled simultaneously with the TOC SIF radiance at 760 nm (as described in section 2.3.3.2).

### 2.3.3. Radiative transfer modelling

*2.3.3.1. Leaf chlorophyll content retrieval by PROSAIL inversion.* Because the leaf chlorophyll $a + b$ content ($C_{ab}$) measured by laboratory chemical analysis was found to be unreliable, we retrieved $C_{ab}$ of experimental plots from their UAS hyperspectral TOC reflectance images through inversion of the PROSAIL radiative transfer model (Jacquemoud et al., 2009). The image GSD was aggregated to 0.08·0.08 m pixel size and spectrally smoothed with a 3 × 3 pixels moving kernel mean filter to increase the signal to noise ratio. As the PROSAIL inversion is sensitive to spatially varying canopy structure, we excluded heterogeneous canopy parts of the image based on information extracted from the canopy DSM (see section 2.2.2, Fig. 1). The DSM raster (GSD = 0.02 m) was spatially resampled to fit the 0.08 m pixel size hyperspectral image. Then a DSM slope image was calculated and pixels with a slope > 35° were excluded (section 2.3.1.1). In a next step, the hyperspectral image was superimposed over the DSM, enabling the spatial match of both raster layers, and the drone image was clipped with the experiment's plot boundaries, reduced by 0.4 m to exclude edge effects, and with the slope mask from the DSM. As a result, only pixels in the experimental plots with a DSM slope ≤ 35° were used in the PROSAIL inversion. Finally, we retrieved $C_{ab}$ with the Automated Radiative Transfer Models Operator (ARTMO) look-up-table inversion tool designed for PROSPECT-D (Féret et al., 2017, 2021) and 4SAIL models (Verrelst et al., 2014). The PROSPECT-D input parameters were adopted from value ranges for wheat listed in Berger et al. (2018) and 4SAIL parameters were based on actual conditions at time of the drone flight and on results from laboratory analysis of the individual plant samples (see Table 2).

**Table 2**
Input parameters used in PROSAIL simulations for retrieval of leaf chlorophyll $a$ + b content.

| Parameter | Values | Unit | Description |
|---|---|---|---|
| **PROSPECT-D** | | | |
| N | 1–2.5 | - | Leaf mesophyll scattering parameter/ leaf structure index |
| $C_{ar}$ or $C_{cx}$ | 0–14.5 | $\mu g \cdot cm^{-2}$ | Total carotenoid content |
| $C_{ab}$ | 0–80 | $\mu g \cdot cm^{-2}$ | Leaf chlorophyll $a$ + b content |
| $C_{Anth}$ | 0–40 | $\mu g \cdot cm^{-2}$ | Total anthocyanin content |
| $C_{bp}$ | 0–100 | - | Brown pigments |
| $C_w$ | 0.001–0.05 | cm | Equivalent water thickness |
| $C_{dm}$ | 0.001–0.01 | $g \cdot cm^{-2}$ | Dry matter content |
| **4SAIL** | | | |
| LAI | 0.45–8 | $m^2 \cdot m^{-2}$ | Leaf area index |
| hspot | 0.01–0.4 | $m \cdot m^{-}1$ | Hotspot parameter |
| ALIA | 10–90 | deg | Average leaf inclination angle |
| skyl | 10–30 | - | Fraction of diffuse radiation |
| tto | 0 | deg | Observer zenith angle |
| Rho soil | measured spectrum | % | Soil reflectance |
| tts | 28.09 | deg | Solar zenith angle |
| psi | 165.51 | deg | Azimuth angle |

*2.3.3.2. DART SIF and APAR simulations.* To investigate and compare normalisation performance of $\epsilon_{F\_FCVI}$ and $\epsilon_{F_{NIRvH1/H2}}$, we created and simulated a virtual 3D scene of our experimental barley plot in a fully controlled environment of DART (v5.8.5). DART simulations of SIF and APAR radiative budgets were carried out for varying canopy LAI, three potentially occurring LADs, and varying leaf optical properties, including joint PSI plus PSII fluorescence quantum efficiency (FQE), simulated with the leaf radiative transfer model Fluspect-Cx (Lamsal et al., 2022; Vilfan et al., 2018). The simulations were executed in the flux tracking radiative transfer mode, without presence of atmosphere, using mean bottom of atmosphere (BOA) solar irradiance as measured with the AirSIF upward looking channel for solar zenith and azimuth angles (SZA and SAA) of the four overflight times on 29th June 2018. Actual values and ranges of leaf biochemical and physical properties were measured in the laboratory (Table 1), or, as for instance of leaf mesophyll structure parameter N, adopted from scientific literature (Jacquemoud et al., 1996). Bare soil ground reflectance was measured in-situ with an optical ASD soil-probe attached with an optical fibre to the ASD FieldSpec-4 spectrometer (Malvern Panalytical Ltd., UK). The virtual infinitely juxtaposed 3D canopy was represented by a 0.6 m high rectangular assembly of equilateral triangular leaves (leaf area of 0.001 $m^2$), distributed homogeneously with varying LAI and LAD. Actual values of the DART scene parameters are listed in Table 3 and detailed DART settings, allowing to reproduce the DART simulations, are available in appendix B. In total, we simulated 45,000 different parameter combinations and stored their SIF and APAR outputs in a MySQL database for further processing.

*2.3.3.3. Estimation of $fAPAR_{green}$ and canopy SIF escape factor.* An estimate of $fAPAR_{green}$ is required to calculate APAR based on the concept of light use efficiency ($APAR = fAPAR_{green}$*PAR; Monteith, 1977). Apart from $C_{ab}$, $fAPAR_{green}$ is driven by LAI, PAR intensity and LAD. $C_{ab}$ was restricted to a narrower range of 20–50 $\mu g.cm^{-2}$, closer to the PROSAIL estimates for the investigated measured experimental plots (Table 1), and $fAPAR_{green}$ was then modelled as a function of LAI for each solar zenith angle (SZA) and for two LADs: i) spherical, representative for non-lodging barley plants, and ii) planophile, typical for lodging plants. The relationship between LAI and $fAPAR_{green}$ was quantified with a self-starting asymptotic regression function (SSasymp, R "stats" package v3.6.2). Unlike exponential functions, the asymptotic function does not produce predictions of values >1, which would not be meaningful for $fAPAR_{green}$. Separate regression functions were fitted to planohile and spherical LADs, and to different SZA corresponding to the time of the airborne sensor overflights (Fig. S1). The quality of the fit was assessed

**Table 3**
Parameters and values used for DART barley plot simulations. More detailed DART settings can be found in the supplementary information Table S1.

| Parameter | Values | Unit | Description |
|---|---|---|---|
| $C_{ab}$ | 10, 25, 40, 55, 70 | $\mu g \cdot cm^{-2}$ | Leaf chlorophyll $a + b$ content |
| $C_{car}$ | 2, 5, 8, 11, 14 | $\mu g \cdot cm^{-2}$ | Leaf carotenoid (total) content |
| $C_{dm}$ | 0.0041* | $g \cdot cm^{-2}$ | Dry matter content |
| $C_w$ | 0.0081* | cm | Equivalent water thickness |
| N | 1.0, 1.5, 2.0, 2.5 | - | Leaf mesophyll structure parameter |
| LAI | 0.5, 1.0, 2.0, 4.0, 8.0 | $m^2 \cdot m^{-2}$ | Leaf area index |
| LAD | spherical, planophile, erectophile | - | Leaf angle distribution |
| Plot x, y | 1, 1 | m | Size of simulated juxtaposed scene |
| Canopy height | 0.6 | m | Canopy height |
| FQE (PSI + PSII) | 0.005, 0.01, 0.02, 0.03, 0.04, 0.05 | - | Fluorescence quantum yield efficiency for photosystems I & II |
| SZA | 38.6, 33, 27.9, 35.26, 47.87 | deg | Solar zenith angle |
| SAA | 122.04, 137.05, 192.11, 229.67, 254.67 | deg | Solar azimuth angle (from north clockwise) |

* Computed as median of the measurements listed in Table 1.

by comparing the observed $fAPAR_{green}$, calculated from DART, to $fAPAR_{green}$ predicted by applying the fitting function of LAI for each modelled SZA and LAD separately (Fig. S2). Consequently, the coefficients describing the asymptotic functions were applied to estimate $fAPAR_{green}$ and APAR of experimental plots of interest. The second component, $f_{esc}$, was modelled as a function of LAI per SZA and LAD in the same way as $fAPAR_{green}$ (Fig. S3 and S4). Resulting $fAPAR_{green}$ and $f_{esc}$, assigned to each plot, were computed as weighted averages according to the percentage of non-lodging and lodging parts of the canopy per plot (as described in section 2.3.1.1). The analysis was conducted in R Statistical Software (v4.0.3; R Core Team, 2021).

Deriving $fAPAR_{green}$ and $f_{esc}$ for the measured data allows for comparing $f_{esc}$ modelled in DART and estimates of $f_{esc}$ based on SIF normalisation with vegetation indices as suggested in Siegmann et al. (2021):

$$fesc \approx \frac{FCVI/NIRvH1/H2}{fAPARgreen}, \quad (5)$$

*2.3.3.4. Relative error of SIF normalisation methods.* Yang et al. (2020) suggested to assess the relative error (RE), i.e., the bias, of the SIF normalisation method using a reference $\epsilon_F$ value. In our case, $\epsilon_{F\_leaf}$ is represented by:

$$\epsilon_{F\_leaf} = \frac{\pi \cdot leaf\ F_{760}}{APAR}, \quad (6)$$

Leaf $F_{760}$ emission is driven by diurnal variations in APAR intensity, and it is complementary to leaf photosynthetic efficiency (i.e., photochemical quenching – PQ) and heat energy dissipation (i.e., non-photochemical quenching – NPQ). Due to the absence of a leaf biochemical photosynthetic model in DART, PQ and NPQ are not modelled and none of the leaf photoprotective adaptations (e.g., chloroplast movement or upregulation of the xanthophyll cycle) is considered in modelled APAR. Additionally, DART-simulated leaf ChlF emissions do not account for microclimatic conditions (e.g., local temperature, humidity, or wind aerodynamics). These factors are nearly constant in a vertical profile of a structurally homogeneous spring barley canopy (height of only 60 cm) and their impact on variability of SIF emissions is, compared to other drivers, negligible. Therefore, a normalisation of leaf $F_{760}$ by APAR modelled in DART produces $\epsilon_{F\_leaf}$ compensating for optical interactions of SIF with canopy structures and soil, as well as leaf biochemical contents with internal leaf anatomy and 3D spatial distributions of modelled foliar components (see Table 3). RE of $\epsilon_{F\_FCVI}$ was subsequently expressed as:

$$RE\ [\%] = \frac{\epsilon_{F_{FCVI}} - \epsilon_{F_{leaf}}}{\epsilon_{F_{leaf}}} * 100, \quad (7)$$

RE of $\epsilon_{F_{NIRvH1/H2}}$ was calculated the same way, just substituting $\epsilon_{F\_FCVI}$ by $\epsilon_{F_{NIRvH1/H2}}$. Additionally, Yang et al. (2020) suggested not to compute RE of $\epsilon_{F\_FCVI}$ for sparse canopies, as the physical theory underlying the $\epsilon_{F\_FCVI}$ concept is valid only for canopies with LAI >1. Thus, RE can be also used for screening purposes, to exclude data points where $\epsilon_{F\_FCVI}$ has too large uncertainty.

## 3. Results

This section is divided into results originating from: i) DART modelling of SIF, specifically $F_{760}$, $\epsilon_{F\_FCVI}$, and $\epsilon_{F\_NIRvH1/H2}$, as functions of canopy biophysical and biochemical traits, and ii) application of those results on the experimental airborne AirSIF and HyPlant SIF data and comparison with the outcomes of DART modelling.

### 3.1. DART modelling

#### 3.1.1. $F_{760}$, PAR, and APAR

The aim of TOC SIF normalisation is to minimize confounding canopy structural effects in the remotely sensed SIF signal, but also to reduce the signal dependency on diurnally changing available PAR and, consequently, APAR. The computed $\epsilon_{F\_FCVI}$, and $\epsilon_{F\_NIRvH1/H2}$ are expected to closely approximate the $F_{760}$ emitted by plant leaves. Both TOC and leaf $F_{760}$ were extracted from the DART simulations of virtual barley canopies. $F_{760}$ increases with increasing LAI (0.5–8) from close to 0 to 14 $mW \cdot m^{-2} \cdot nm^{-1} \cdot sr^{-1}$ at the canopy level, while it is reaching values 23 $mW.m^{-2}.nm^{-1}.sr^{-1}$ at the leaf level (Fig. A1). Furthermore, canopies with planophile LAD showed a significantly different linear regression slope compared to spherical and erectophile canopies. For all cases, TOC $F_{760}$ is smaller than leaf $F_{760}$, with slightly varying slopes (0.498–0.528), with slope increasing with increasing LAI. For LAI ≥ 2, TOC $F_{760}$ is in general, 50 % lower than $F_{760}$ emitted from the leaves, which clearly indicates a strong influence of canopy architecture on TOC $F_{760}$.

The simplest normalisation of TOC $F_{760}$ is its division by PAR, where PAR is used as a proxy of the canopy APAR. Fig. 2A shows the diurnal course of PAR according to the data acquisition times and SZA in the field study. The variability of DART-simulated APAR showed that LAI <2 leads to APAR ≤50 % of the observed PAR. Other factors causing the variation of APAR are LAD and $C_{ab}$, with planophile canopies inducing higher APAR than erectophile canopies (results not shown). In addition, when looking at the ratio of PAR to APAR in Fig. 2B it is apparent that this ratio is nearly constant over the day for high LAI >2 but varies over the day for LAI <2. Fig. 2 clearly demonstrates that PAR is, in most cases, not a sufficient approximation of APAR. Especially in sparse canopies, PAR is considerably larger than the amount of energy available for photosynthesis at the leaf level due to neglection of canopy architecture and soil background.

#### 3.1.2. Relative errors of $F_{760}$ normalisation approaches

Yang et al. (2020) suggested the RE of FCVI to be used as a screening tool for excluding cases where the assumption of the physical theory behind the SIF normalising index is invalid, e.g., sparse canopies (see 2.3.3.4). Since the dataset modelled in DART had freely varying variables, e.g., N-number and FQE of the photosystems I + II, we could determine specific RE thresholds for tested indices from our simulations (Fig. 3). The FCVI threshold was later applied to classify reliability of the airborne observations (Fig. 7). Fig. 3 shows the relative error (RE) of $\epsilon_{F\_FCVI}$ and $\epsilon_{F_{NIRvH1/H2}}$ per actual value of the index, coloured by LAI. The RE increases exponentially for low FCVI and NIRv/H1/H2 values

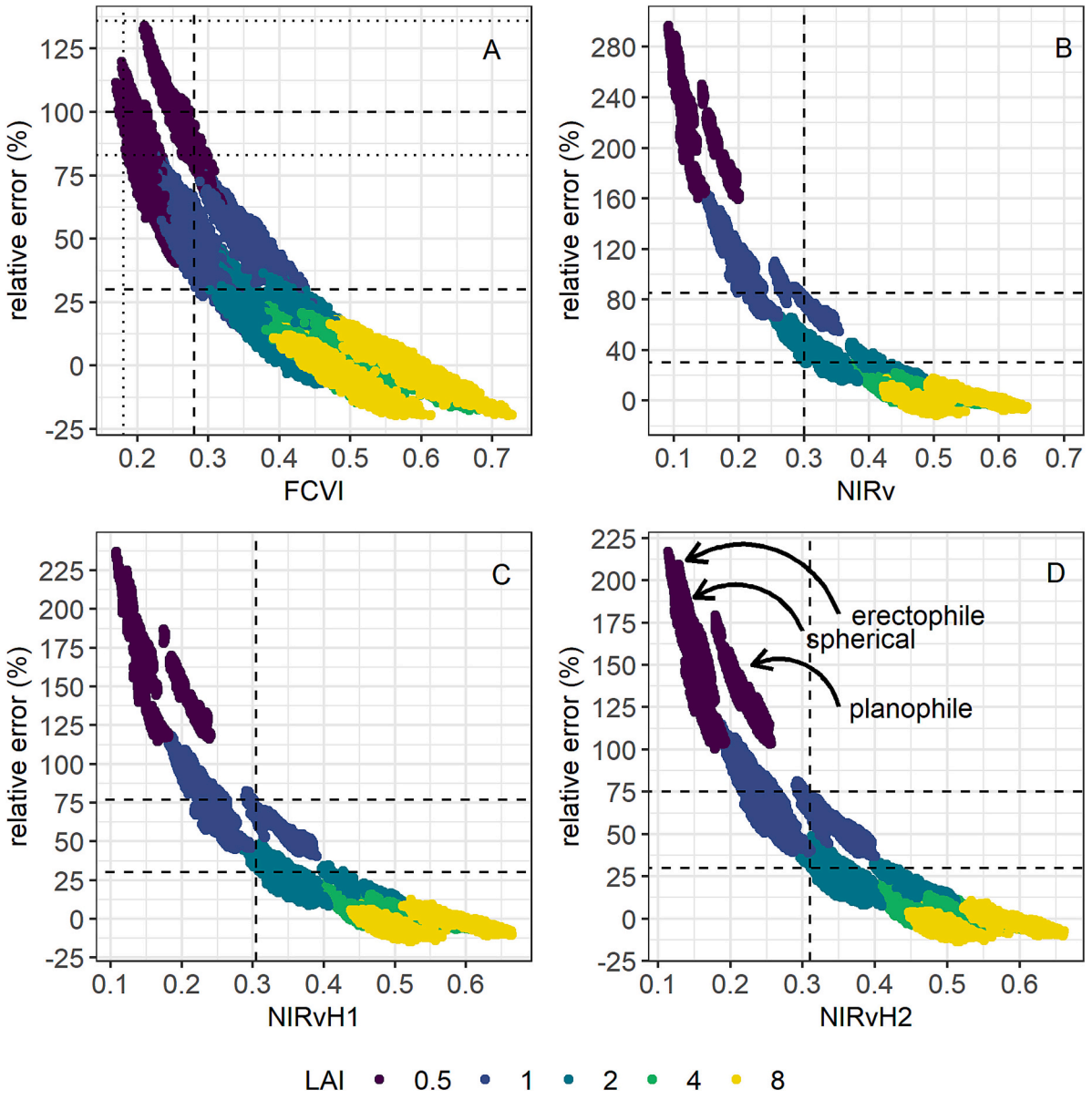


**Fig. 3.** (A) Relative error (RE) for FCVI, (B) NIRv, (C) NIRvH1, and (D) NIRvH2 based fluorescence efficiency per index value, calculated for barley canopies simulated in DART after Yang et al. (2020). The dashed lines show the RE range at 30 % RE and the dotted lines represent the RE range at FCVI threshold 0.18 as suggested by Yang et al., 2020.In B-D: RE of NIRv, NIRvH1, NIRvH2- based fluorescence efficiency and respective RE at 30 %.

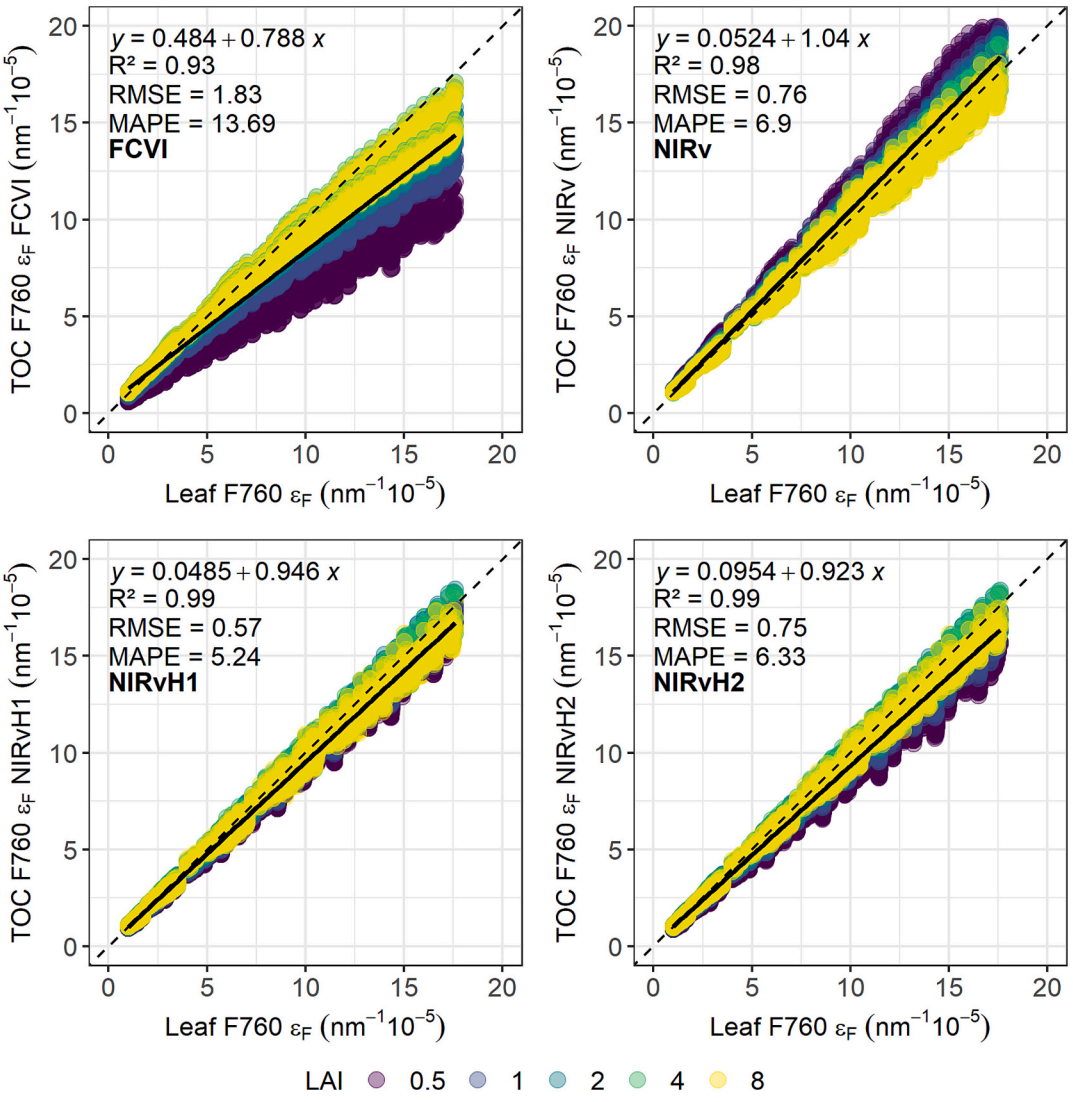


**Fig. 4.** Comparison of $F_{760}$ efficiency factors calculated from TOC $F_{760}$ $\epsilon_{F\_FCVI}$ and $\epsilon_{F_{NIRvH1/H2}}$ against $\epsilon_{F\_leaf}$ (see Eq. 6). Data is shown for 14:00 (27.9°) and 17:00 (47.87°) CEST (SZA) and coloured by LAI 0.5–8. The dashed line indicates the 1:1 line, the black line is the linear regression line for all LAI combined, and $R^2$ indicates the coefficient of determination, RMSE is the root mean square error in $nm^{-1}$ and MAPE is the mean absolute percent error. Input values for the DART simulations are listed in Table 3.

(<0.3). For moderate to high FCVI and NIRv/H1/H2 values (>0.3) RE is higher for planophile LAD than for spherical and erectophile canopies. Yang et al. (2020) identified a FCVI value of 0.18 as a practical threshold to exclude estimates of $\epsilon_{F\_FCVI}$ with a relative error > 30 % (dotted horizontal lines in Fig. 3A). For our simulated data, the 0.18 FCVI threshold corresponds to a RE of 80–130 % (dotted vertical line in Fig. 3A). To retain the recommended minimum of 30 % RE cut-off, we set a threshold of 0.28 and 0.3–0.31 for NIRv/H1/H2, respectively (dashed vertical lines in Fig. 3). These thresholds equate to canopies with LAI of 1–2, depending on LAD. Significantly higher errors occurred for planophile canopies, i.e., RE up to 100 % for FCVI and 85 % for NIRv/H1/H2, respectively.

### 3.1.3. $F_{760}$ efficiency

To address and minimize the influence of canopy architecture and PAR/APAR, we applied the $\epsilon_{F\_FCVI}$ and $\epsilon_{F_{NIRvH1/H2}}$ normalisation approaches on DART simulations as described in 2.3.2. Fig. 4 shows a comparison of efficiency factors against $\epsilon_{F\_leaf}$ for the smallest and largest simulated SZA, coloured by simulated LAI. For $\epsilon_{F_{NIRvH1/H2}}$, plotted points are located close to the 1:1 line ($R^2$ 0.98–0.99) with slopes close to 1 and intercepts <0.05. $\epsilon_{F\_NIRvH1}$ tracks $\epsilon_{F\_leaf}$ best with the lowest root mean square error (RMSE) of 0.55 $nm^{-1}10^{-5}$. Additionally, $\epsilon_{F\_NIRvH1}$ shows no dependency on LAI, whereas $\epsilon_{F\_NIRv}$ overestimates $\epsilon_{F\_leaf}$ for low LAI <1 and $\epsilon_{F\_NIRvH2}$ underestimates $\epsilon_{F\_leaf}$ for LAI <1. Therefore, $\epsilon_{F\_NIRvH1}$ was chosen for further analysis. For $\epsilon_{F\_FCVI}$, Yang et al. (2020) observed a strong dependency on low LAI. Results of our 3D DART simulations confirmed that FCVI underestimates $\epsilon_{F\_leaf}$ ($R^2$ 0.93) with a slope of 0.79 (Fig. 4). The underestimation is larger for canopies with LAI <2. Hence, $\epsilon_{F\_NIRvH1}$ was found to be least sensitive to vegetation canopy LAI changes and tracking $\epsilon_{F\_leaf}$ most reliably.

Fig. 5 shows the influence of LAI and LAD on TOC $F_{760}$ divided by APAR, $\epsilon_{F\_NIRvH1}$, $\epsilon_{F\_FCVI}$ in higher detail. In comparison with TOC $F_{760}$ divided by APAR, both $\epsilon_{F\_NIRvH1}$ and $\epsilon_{F\_FCVI}$ compensate well for the effects of LAI and LAD when LAI is 2 or larger. For LAI equal to 0.5 and 1 (not shown), $\epsilon_{F\_NIRvH1}$ is clearly superior to $\epsilon_{F\_FCVI}$. It is noticeable that the relationship between $\epsilon_{F\_leaf}$ and $\epsilon_{F\_FCVI}$ becomes non-linear for high $\epsilon_F$, which is not the case for $\epsilon_{F\_NIRvH1}$.

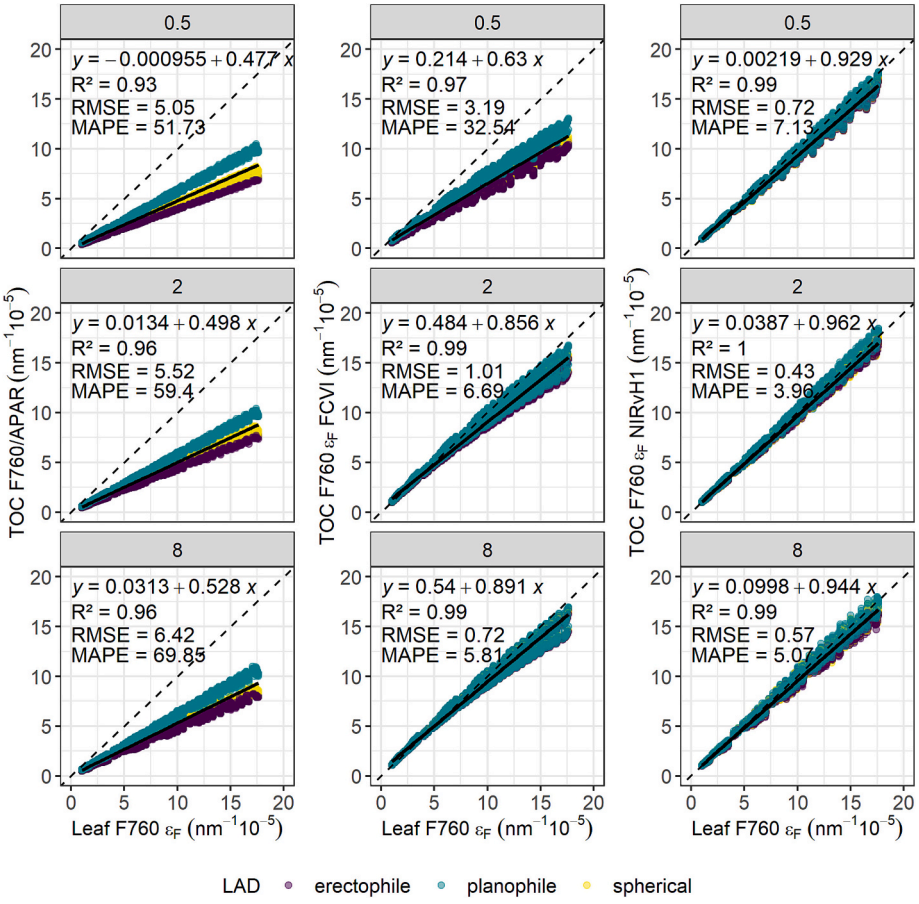


**Fig. 5.** Comparison of DART simulated leaf level $F_{760}$ efficiency factors $\epsilon_{F\_leaf}$ against TOC $F_{760}$ normalised by APAR, $\epsilon_{F\_FCVI}$ and $\epsilon_{F\_NIRvH1}$ calculated from TOC $F_{760}$ for LAI 0.5–8 (indicated at the top of each panel), and coloured according to leaf angle distribution (LAD) functions. The dashed line indicates the 1:1 line, the black line is the linear regression line for all LAD combined, and $R^2$ indicates the coefficient of determination. RMSE stands for root mean square error, and MAPE is the mean absolute percent error. Input values for the DART simulations are listed in Table 3.

### 3.2. Aerial observations

Fig. 6 displays an overview of the experiment field with AirSIF footprints acquired at 15:30 CEST and projected over the nine sampled barley plots (panel A). Only the footprints that have been included in the analysis after the spatial filtering process described in 2.3.1.4 are shown. Panel B shows HyPlant TOC $F_{760}$ for the flight conducted at 15:00 CEST with a pixel size of 0.5·1 m. Panels C and D show $\epsilon_{F\_FCVI}$ and $\epsilon_{F\_NIRvH1}$ respectively, computed per pixel of the same flight raster data. Clear differences in $F_{760}$ can be observed between plots, with higher $F_{760}$ occurring in plots containing larger portion of green than senescent biomass (see RGB representation in panel A). This general pattern persists also in the map of $\epsilon_{F\_FCVI}$ (panel C), however, pixels at the plot edges with prevailing green biomass show increased $\epsilon_{F\_FCVI}$ compared to the pixels in plot centres. The map of $\epsilon_{F\_NIRvH1}$ (panel D) shows, in general, similar patterns when compared to $\epsilon_{F\_FCVI}$. Yet, very high values of $\epsilon_{F\_NIRvH1}$ at edges of experimental plots and over bare soil, indicated by the yellow-coloured pixels, suggest unrealistic overestimates for barley pixels mixed spectrally with bare soil. For further analysis, AirSIF and HyPlant measurements were integrated per experiment plot. The mean value per plot was used for AirSIF data, whereas the pixel aggregation approach described in section 2.2.3 was employed for HyPlant $F_{760}$ images.

The comparison of the efficiency factors pooled for all observation times/SZA and both aerial sensors is shown in Fig. 7 (Panel A). The TOC SIF efficiencies are coloured by sensor type, shape of symbols indicates FCVI values $\leq$0.28 or $>$ 0.28 according to the relative error threshold established in Fig. 3. Only two datapoints showed a FCVI $<$0.28. HyPlant observations from high overflights deviated stronger than UAS observations and low HyPlant flights. Panel B shows the same relationship of the modelled data for comparison after restricting it to the range of measured data of LAI 1–8, LAD planophile or spherical, $C_{ab}$ 20–40 μg·cm$^{-2}$, and $\epsilon_{F_{FCVI}/NIRvH1}$ $\leq$10 nm$^{-1}$·10$^{-5}$ (see also Fig. S7). Compared to the modelled data ($R^2$ = 0.98) a similarly strong but slightly weaker correlation ($R^2$ = 0.93) was found and errors increase in the measured data, indicated by a higher RMSE and mean absolute percent error (MAPE). FQEs shown in panel B suggest that the FQEs of measured data ranged between 0.01 and 0.03.

To evaluate diurnal courses measured from the aerial platforms AirSIF and HyPlant, all sampling plots are pooled per overflight and presented as TOC $F_{760}$ and its normalisations by APAR and the two efficiency approaches. Fig. 8 shows values from the nine experimental plots (depicted in Fig. 6) sorted by time of overflight and distinguishing low (350 m) and high (680 m) overflights of HyPlant. The diurnal course of mean canopy APAR has been added for a better orientation. The overall TOC SIF, displayed in panel A, is lower in the late morning than in the afternoon and indicates that $F_{760}$ reaches the highest diurnal emissions about 1–2 h after solar noon, which is also the case for all three normalised datasets (panels B—D). The variance in the high-altitude HyPlant overflights is the largest (grey), particularly for the overflight at 14:45 CEST. Remaining TOC SIF values range predominantly between 0.5 and 1.5 mW·m$^{-2}$·nm$^{-1}$·sr$^{-1}$. After normalising TOC SIF by APAR (panel B), the overall data distribution pattern stays similar, especially from late morning until 14:00 CEST. In comparison to panel A, the afternoon values are slightly shifted, especially for the 17:00 CEST overflight (see also Fig. S10). Similarly, $\epsilon_{F\_FCVI}$ (panel C) and

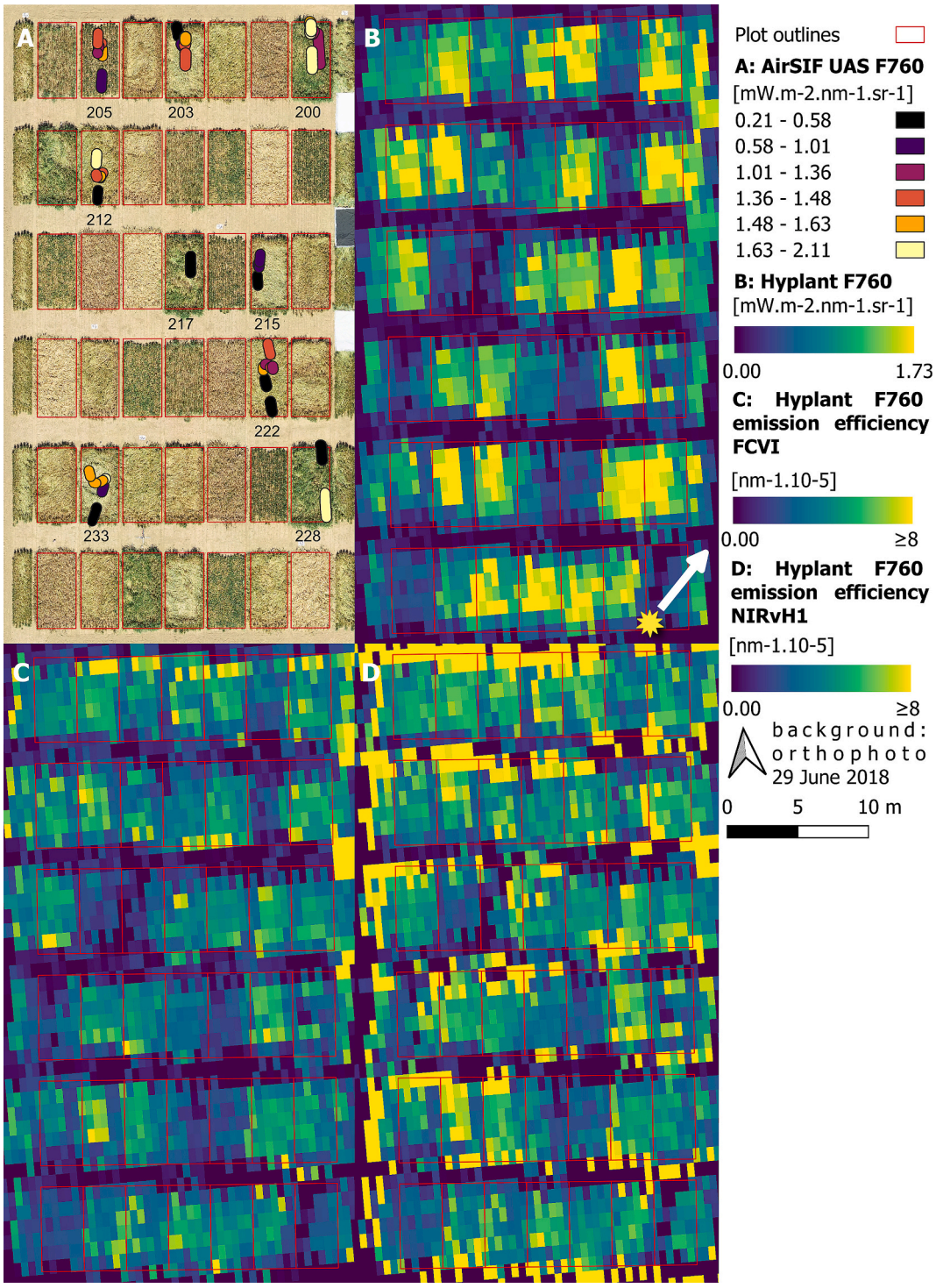


**Fig. 6.** Barley experimental field on 29 June 2018 with plot outlines shown in red depicting: (A) AirSIF drone $F_{760}$ measurements for the flight conducted at 15:30 CEST with orthophoto in the background (pixel size of 0.03 m) and plot IDs (see Table 1), (B) HyPlant $F_{760}$ flight at 15:00 CEST, pixel size of 0.5·1 m, acquired at 350 m above ground level, (C) $\epsilon_{F\_FCVI}$ computed from the same HyPlant flight, and (D) $\epsilon_{F\_NIRvH1}$ also from the same HyPlant flight. The arrow and sun symbol indicate the solar azimuth angle at 15:00 CEST. (For interpretation of the references to colour in this figure legend, the reader is referred to the web version of this article.)

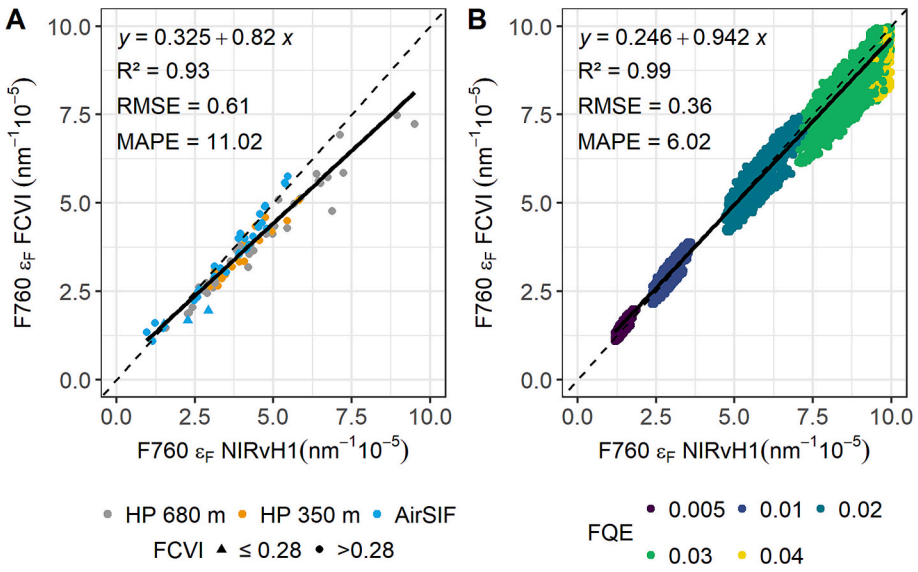


**Fig. 7.** (A) Comparison of $F_{760}$ efficiency factors $\epsilon_{F\_FCVI}$ and $\epsilon_{F\_NIRvH1}$ for the barley experiment plot measurements, coloured by sensor type and shape of symbols corresponds to FCVI class according to the relative error threshold (FCVI = 0.28) determined in simulated data (Fig. 3; n = 90). (B) $F_{760}$ efficiency factors $\epsilon_{F\_FCVI}$ and $\epsilon_{F\_NIRvH1}$ from DART simulated data restricted to the range of measured data 0–10 $nm^{-1}{\cdot}10^{-5}$. Visualised data are constrained to LAI 1–8, spherical and planophile LAD, $C_{ab}$ 20–40 $\mu g{\cdot}cm^{-2}$, and coloured by fluorescence quantum yield (FQE). The dashed line indicates the 1:1 line, the black line is the linear regression line, and $R^2$ indicates the coefficient of determination, RMSE stands for the root mean square error, and MAPE for mean absolute percent error.

$\epsilon_{F\_NIRvH1}$ show the largest change on the diurnal distribution in the late afternoon. Note that the variability per flight is driven by contrasting barley phenotypes and corresponding crop development stages and uncertainties in the measured radiances and SIF retrieval. To better assess the effects of $\epsilon_{F\_FCVI}$ and $\epsilon_{F\_NIRvH1}$, Fig. 9 shows the same data as Fig. 8 but plotted against TOC $F_{760}$. In this visualisation, a weaker relationship indicates decoupling from TOC $F_{760}$. $\epsilon_{F\_NIRvH1}$ shows a larger deviation from TOC $F_{760}$, indicating a slightly larger effect on the diurnal course of the data.

Finally, we assessed $f_{esc}$ calculated from Eq. 5 in a direct comparison against $f_{esc}$ in nadir direction of green vegetation simulated in DART ($f_{esc}$ DART) (Fig. 10A). $f_{esc}$ FCVI strongly differs from $f_{esc}$ DART and the non-systematic deviation is driven by LAI, combined with a systematic bias caused by FQE and LAD (see Fig. S11). $f_{esc}$ NIRvH1, in turn, tracks $f_{esc}$ DART closely ($R^2$ = 0.88, RMSE = 0.03) (Fig. 10B). In the case of measured data, we found a close match ($R^2$ = 0.81) between $f_{esc}$ FCVI and $f_{esc}$ NIRvH1, but the $f_{esc}$ values were in general lower than in simulated data when restricted to the range of measured LAI, LAD and $C_{ab}$ (see Fig. 10C-D).

## 4. Discussion

### 4.1. Performance and limitations of FCVI and NIRvH1 SIF efficiency

#### 4.1.1. Modelled outcomes

In this study, we used a radiative transfer modelled dataset and TOC SIF in-situ data from two independent airborne sensor platforms to study the impact of canopy structure on the relation between leaf and TOC $F_{760}$. Specifically, we studied the performance and limitations of the FCVI and NIRv-based $F_{760}$ normalisation approaches in cereal crop canopies.

In the DART simulations, $F_{760}$ emitted by all leaves in the canopy was in general twofold higher than $F_{760}$ at the top of the canopy, which is in line with result demonstrated by previous studies (Malenovský et al., 2021; Yang and van der Tol, 2018; Zhang et al., 2016). Both TOC $F_{760}$ and leaf $F_{760}$ are driven by APAR, which is mainly dependent on solar zenith angle (SZA) and LAI (Fig. 2). APAR is not stable over the course of the day, which indicates that normalisation of TOC $F_{760}$ by PAR or APAR is insufficient for revealing relative changes of the diurnal course of leaf $F_{760}$. To find the most suitable $F_{760}$ normalisation approach for crop canopies with varying structure, we compared the performance of TOC $\epsilon_F$ (Eqs. 3, 4) of FCVI, NIRv, NIRvH1 and NIRvH2 against $\epsilon_{F\_leaf}$. DART radiative budget simulations allow to accurately approximate leaf $F_{760}$ and compare $\epsilon_F$ approaches. Based on the DART simulated results, performance of $\epsilon_{F\_NIRvH1}$ is superior to the other NIRv-based approaches and $\epsilon_{F\_FCVI}$. Not only does it match $\epsilon_{F\_leaf}$ very closely, but the relationship is also least biased compared to the other approaches (see Figs. 4 & 5).

It must be noted that fluorescence quantum yield efficiency (FQE) was varied between 0.005 and 0.05 in DART simulations (personal communication P. Yang), where 0.05 refers to the maximum realistic FQE that is not likely to be reached during most days. Additionally, LAD and LAI influenced the relationship between $\epsilon_{F\_FCVI}$ and $\epsilon_{F_{NIRvH1/H2}}$, with LAI below 2 (i.e., FCVI <0.28, NirvH1/H2 0.3–0.31) producing $\epsilon_{F\_FCVI}$ or $\epsilon_{F_{NIRvH1/H2}}$ RE ≥30 %, respectively (Fig. 3). This observation has been confirmed by the theoretical deduction of FCVI in Yang et al. (2020). In their study, they suggested to exclude cases where $\epsilon_{F\_FCVI}$ is not reliable, by setting an FCVI threshold of 0.18. RE for low FCVI values, simulated in the SCOPE model with a realistic soil background, was found to be negative (Yang et al., 2020). In our study, we observed mainly positive RE for FCVI and NIRvH1/H2 simulated with the soil spectra measured at the study site (and for a black soil, see Fig. S5). RE became negative for LAI of 8 but never reached more than 20 %. The explanation is that for very low FCVI $\epsilon_F$ modelled in SCOPE are higher compared to $\epsilon_F$ from DART, causing the RE to be positive in DART and negative in SCOPE. However, these are extreme cases, which are not likely observed in in-situ data.

In general, there is a difference between both studies in the magnitude of observed $\epsilon_{F\_FCVI}$, which is ~0.25–2.5·$10^{-5}$·$nm^{-1}$ in SCOPE compared to 1–17·$10^{-5}$·$nm^{-1}$ in DART. This difference can be partially explained by the simulation input parameter ranges. In the SCOPE simulations, the SZA were 30–60° and viewing zenith angles of 0–60°, while PAR was 100–800 $W{\cdot}m^{-2}$. In the DART simulations, solar and viewing angles were constrained to the range of our field measurements, i.e., SZA of 28–50°, nadir viewing zenith angles of 0°, and PAR 300–420 $W{\cdot}m^{-2}$. Since additional 49 sensor viewing zenith angles were modelled in DART, we computed $F_{760}$ efficiency factors for the viewing directions closest to the hotspot (i.e., the viewing direction closest to SZA and SAA)

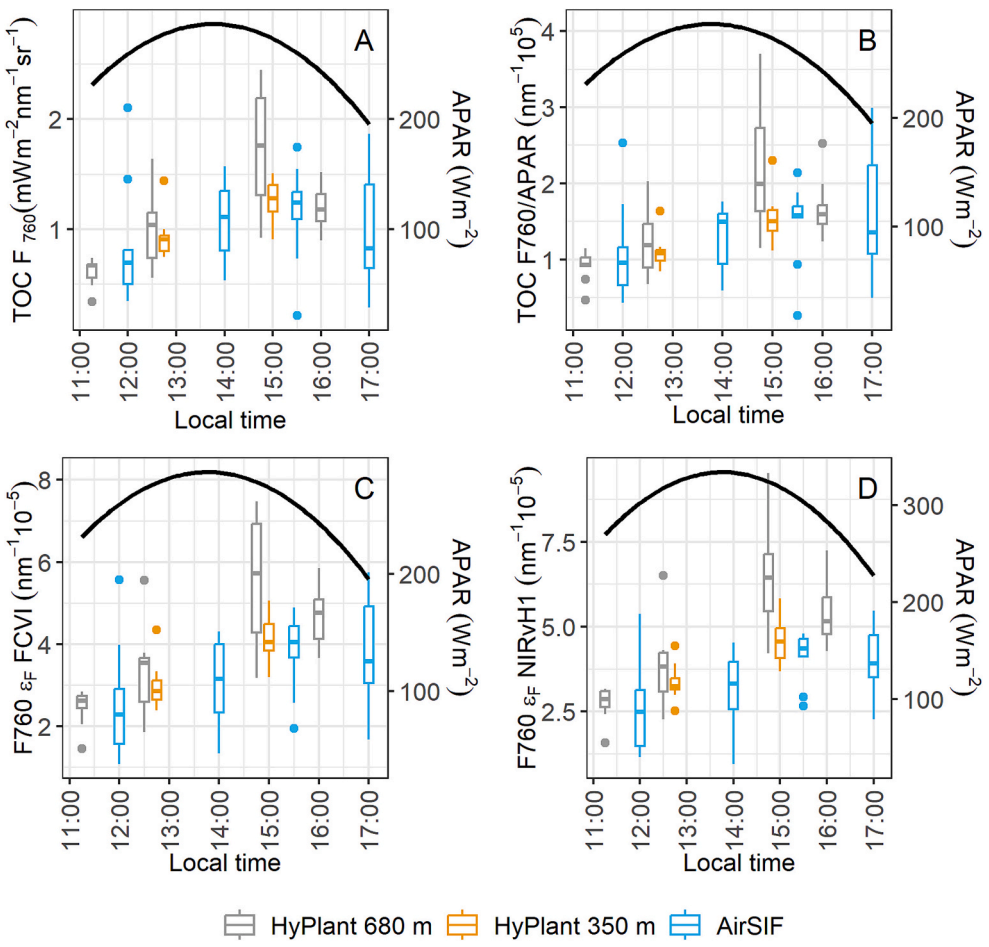


**Fig. 8.** Diurnal observations of TOC $F_{760}$ acquired by HyPlant flying at 350 and 680 m above ground (in orange and grey, respectively), and AirSIF flying at 8–10 m above ground (blue). Overflights were conducted between 11:15 and 17:00 CEST on 29 June 2018. Panels show: (A) TOC $F_{760}$, (B) TOC $F_{760}$ normalised by APAR, and (C) $F_{760}$ normalised by the efficiency factors $\epsilon_{F\_FCVI}$ and (D) $\epsilon_{F\_NIRvH1}$. Mean APAR (black solid line) is displayed on the second y-axis. Box plots show the average of 9 experimental plots, which consisted of different barley varieties (cf. Fig. 6). (For interpretation of the references to colour in this figure legend, the reader is referred to the web version of this article.)

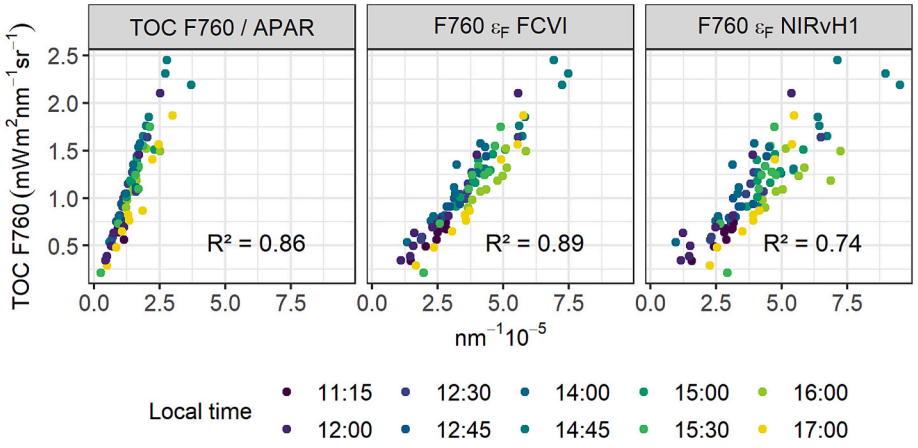


**Fig. 9.** The same diurnal observations of TOC $F_{760}$ are shown as in Fig. 8, comparing TOC $F_{760}$ (y-axis) against TOC $F_{760}$ normalised by APAR (left), normalised by the efficiency factors $\epsilon_{F\_FCVI}$ and $\epsilon_{F\_NIRvH1}$ (x-axis), coloured by data acquisition time.

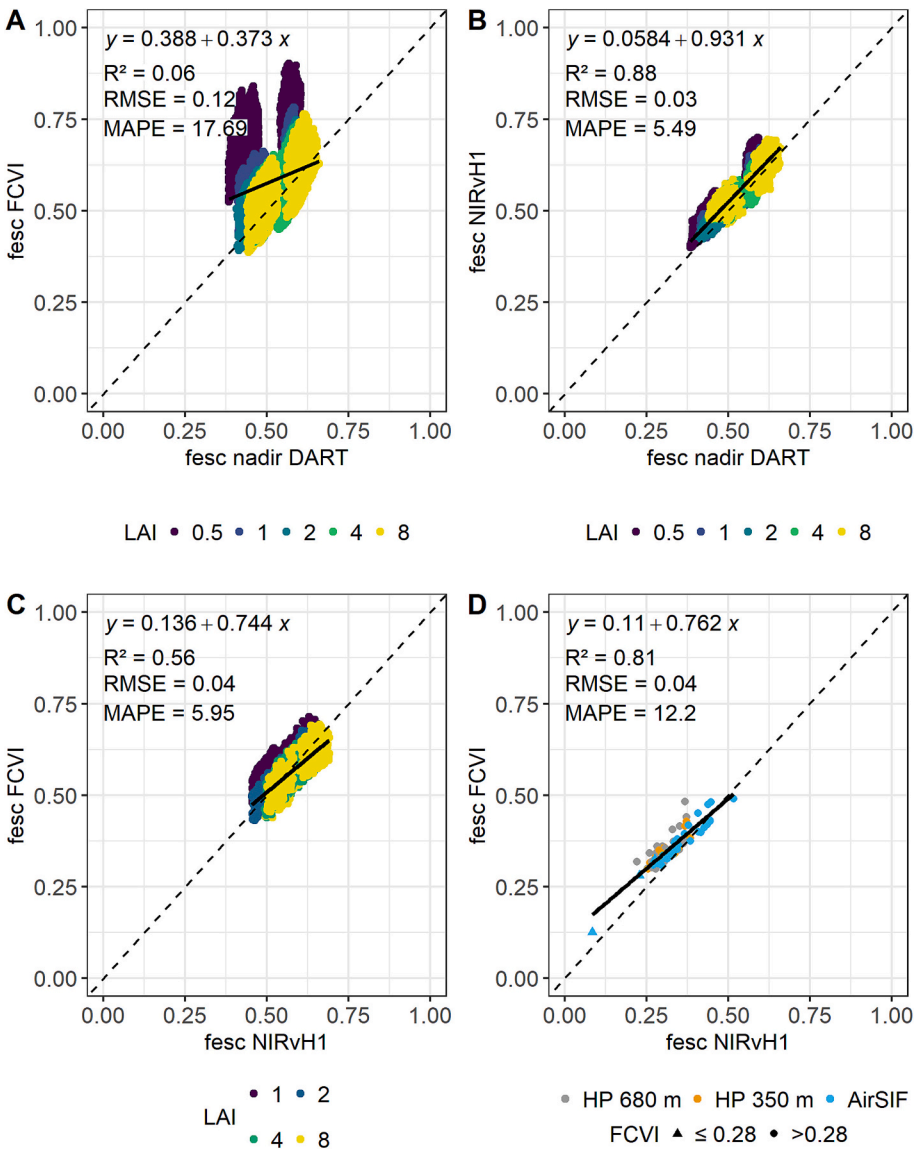


**Fig. 10.** $F_{760}$ escape fractions ($f_{esc}$) for modelled data: (A) nadir $f_{esc}$ against estimated $f_{esc}$ FCVI (see Eq. 5) both simulated in DART, (B) nadir $f_{esc}$ against estimated $f_{esc}$ NIRvH1 both simulated in DART, (C) estimated $f_{esc}$ FCVI and NIRvH1 both simulated in DART but restricted to the range of measured data, and (D) $f_{esc}$ FCVI and NIRvH1 both retrieved from measured data, and coloured by sensor and flight altitude (HP stands for HyPlant, the shape seperates FCVI <> 0.28).

and darkspot (i.e., opposite to hotspot), to assess performances of FCVI and NIRvH1 for the three most oblique simulated SZA (Appendices C and D). Comparable RMSE and MAPE to the nadir direction were observed for near hotspot and darkspot for both $\epsilon_{F\_FCVI}$ and $\epsilon_{F\_NIRvH1}$. Additionally, no significant differences were found between the near-hotspot and near-darkspot $F_{760}$ efficiency factors, which means both indices are able to correct for structural effects of prevailingly sunlit and shaded canopies, observed under viewing zenith angles up to 50°. Yet, as in nadir simulations, the FCVI correction underperformed in the case of off-nadir oblique scenarios with LAI = 0.5. It should be noted that there are methodological differences between the two canopy models. SCOPE is a 1D four-flux radiative transfer model with a canopy represented by a turbid medium filled with infinitely small leaves (Yang et al., 2021a), whereas DART is a discrete 3D multi-flux model working with canopies built out of geometrically explicit leaves of realistic sizes and physically modelled shadows (Regaieg et al., 2021).

There are also differences between our study and Zeng et al. (2021) in the results of $\epsilon_{F_{NIRvH1/H2}}$ that can be explained as follows. First, the soil measured in our experiment field was brighter (reflectance 0.3 at 800 nm) compared to Zeng et al. (2021) with reflectance 0.1–0.22 at 800 nm. In our study we modelled LAI up to 8 as opposed to maximum LAI of 5 in Zeng et al. (2021). We modelled the Cab range from 10 to 70 $\mu g \cdot cm^{-2}$ in comparison to 20–100 $\mu g \cdot cm^{-2}$ in Zeng et al. (2021). Finally, we varied N-number from 1 to 2.5, whereas Zeng et al. fixed N-number at 1.4. Despite these differences, we observed, similarly to Zeng et al. (2021), that NIRv is influenced by the soil background more than NIRvH1 or H2.

In conclusion, results in this study confirmed that $\epsilon_{F\_FCVI}$ can compensate most of the canopy structural influences for canopies with LAI $\geq$ 2. The $\epsilon_{F\_NIRvH1}$ normalisation is more accurate but computationally more complex, intensive, and time consuming and requires hyperspectral observations of soil reflectance. $\epsilon_{F\_NIRvH2}$ could serve as a compromise, as the computation is simpler, and it was performing only slightly worse than $\epsilon_{F\_NIRvH1}$. It should be noted that dynamic and complex variations of leaf $F_{760}$ efficiency occur as a function of PAR and other leaf biochemical photoprotective mechanisms, causing changes in leaf photosynthetic and consequently fluorescence quantum efficiencies. These dynamics are not present in DART and had to be supplied as a range of predefined FQEs.

#### 4.1.2. Measurements from drone and aircraft platforms

To evaluate the advantages and shortcomings of $\epsilon_{F\_FCVI}$ or $\epsilon_{F\_NIRvH1}$, we applied both approaches to remotely sensed SIF observations acquired from different sensors and platforms. These datasets had, however, the following limitations. First, the canopies' architectures within the experimental barley plots were inhomogeneous due to partially lodging plants, caused by an early ripening. We attempted to take the canopy structure into account by calculating the percentage of non-lodging and lodging canopy per plot and assigning a weighted average of $fAPAR_{green}$ and ESC to every plot(see section 2.3.3.1).

Second, we could observe only nine experimental plots with the drone-based sensor AirSIF, due to the maximal drone flight time of only 10–15 min, and due to the necessity to collect several measurements over each plot. This approach ensured enough measurements close to the plot centre, allowing for a scientifically sound statistical analysis. Yet, some measurements, located at the edge of a plot because of the limited drone navigation accuracy, had to be discarded.

Third, only a limited number of pixels was located in each plot due to the relatively large GSD of HyPlant airborne images, i.e., 1·0.5 m and 1·1 m, with respect to the barley plot size of 3·6 m. Consequently, small inaccuracies in georeferencing could lead to deviations in spectral signatures. The risk of these inaccuracies was minimised by extracting plot pixels from a vector file directly drawn onto the HyPlant image, while excluding pixels along the plot edges, and by applying spatial aggregation techniques (see section 2.3.1.5).

Data from HyPlant flights at 680 m AGL presented the highest variability, similar to Krämer et al. (2021). During the investigated day, TOC $F_{760}$ increased and decreased with PAR/APAR as expected, however, only a little decrease was observed in the afternoon (Fig. 8). It should be mentioned that TOC $F_{760}$ tends to decrease less in mature canopies (Campbell et al., 2019), which is the case of our measurements. Krämer et al. (2021) found a stronger afternoon decrease of TOC $F_{760}$ in neighbouring wheat plots of an earlier phenological stage. When comparing TOC $F_{760}$ normalisation by APAR, $\epsilon_{F\_FCVI}$, and $\epsilon_{F\_NIRvH1}$, only little changes in the diurnal pattern were observed and the impact was strongest on the afternoon observations. A stronger effect of TOC $F_{760}$ normalisation was expected but was not observed due to the heatwave causing early ripening of the barley crops. The early ripening led to a reduction in TOC $F_{760}$ and additionally larger phenological variability among barley cultivars. It should be noted that calculation of APAR for measured data required fAPAR estimates, which were generated from a statistical model fitting based on LAI. Thus, inaccuracies in measured LAI impact the estimation of APAR.

Our results confirmed the statistically significant agreement between $\epsilon_{F\_FCVI}$ and $\epsilon_{F\_NIRvH1}$ (Fig. 7A; $R^2 = 0.93$) in the measured data, which is comparable to the DART-modelled results restricted to the value ranges of the measured data (Fig. 7B; $R^2 = 0.99$). Nevertheless, Fig. 8 shows that the normalisation approaches had somewhat limited effect on the large variability that was revealed for data acquired with both platforms during different overflights throughout the day. The closest agreement was found for HyPlant acquisitions at 350 m altitude and AirSIF measurements taken at 12/13:00 and 15/15:30 CEST, respectively. No further quantitative comparison of drone and aircraft was attempted data because of the limited number of observed plots ($n = 9$) (see Fig. S9 for plot-level data).

Finally, we observed a discrepancy between $f_{esc}$ estimated from measured data and radiative transfer simulations with NIRvH1 and FCVI. Since $f_{esc}$ for measured data relies on correct estimations of LAD and LAI used to calculate fAPAR in the form of lookup tables (see Fig. S1, S3), uncertainties in estimating fAPAR propagate into $f_{esc}$ estimation (Yang et al., 2021b). On the other hand, TOC $F_{760}$ modelled in DART may be higher than what was observed in our in-situ data. For instance, Xu et al. (2021) observed a lower $f_{esc}$ simulated in SCOPE than $f_{esc}$ estimated with FCVI from measured data in potato crops.

### 4.2. Limitations and general remarks

The presented results show a detailed analysis for a single crop type of four structurally different barley cultivars. Consequently, the implications of our findings cannot be directly transferred to structurally different crop types or plant functional types, especially those containing woody elements (i.e., shrubs and trees). One reason is that estimating LAI, LAD, and foliage clumping characteristics for tree canopies at such a high spatial resolution as applied in this study is challenging. Our results included simulations of geometrically explicit leaves with modelled shadows, but no specific foliage clumping was included, as it is not expected to be significant for cereal canopies of later growth stages. Consequently, the results are not applicable to highly clumped canopies either. Transferability to grasslands is, however, likely due to the similarity in canopy structure.

Our study is systematically comparing two types of TOC $F_{760}$ normalisation approaches that have been published recently (Yang et al., 2020; Zeng et al., 2021). Since the publication of both approaches, studies that apply these approaches have been conducted, but none of them systematically assessed their strengths and weaknesses (Merrick et al., 2021; Nagy et al., 2024; Wu et al., 2023). Yang et al. (2020) and Siegmann et al. (2021) assessed some performance of FCVI, which is partially confirmed and further extended by results of our study. We confirmed its limited applicability to low LAI with an independent radiative transfer model but found a different threshold for reliability of FCVI (0.28 as opposed to 0.18). Finally, it must be noted that our study is focussed on finding the most reliable method to estimate $\epsilon_{F\_leaf}$ for high spatial resolution data. Estimation of GPP, as attempted in Yang et al. (2023) or Dechant et al. (2022), is beyond the scope of this study.

## 5. Conclusions

The discrete anisotropic radiative transfer modelling of canopy bidirectional reflectance factor, APAR and SIF radiative budgets was found to be an efficient tool for testing performances and assessing limitations of two canopy SIF efficiency standardisation methods in the case of a spring barley experiment. On one hand, it enabled us to investigate robustness of the $\epsilon_{F\_FCVI}$ and $\epsilon_{F_{NIRvH1/H2}}$ normalisation, which employ the FCVI and NIRv/NIRvH1/H2 optical indices as a spectral-invariant reflectance-based proxy compensating for canopy structural impacts. On the other hand, DART facilitated computation of the $F_{760}$ nadir escape probability factor $f_{esc}$ for 3D virtual barley canopies and estimation of fAPAR through lookup tables that could be applied to in-situ data of experimental fields from independent drone and airborne SIF observations.

Results of this study suggest that $\epsilon_{F_{NIRvH1}}$ approximates $\epsilon_{F_{leaf}}$ accurately, even in sparse canopies with a low LAI. $\epsilon_{F\_FCVI}$ is a suitable tool for normalising TOC $F_{760}$ emitted by agricultural crops with canopy LAI $\geq$2. Unlike $f_{esc}$ NIRvH1, we observed a biased relationship between $f_{esc}$ FCVI and $f_{esc}$ DART, non-systematically influenced by LAI and systematically influenced by FQE and LAD. In those cases, the overestimation of $f_{esc}$ FCVI is causing an underestimation of $\epsilon_{F\_FCVI}$. Nevertheless, when applied to the diurnal airborne in-situ observations, both $\epsilon_{F_{NIRvH1}}$ and $\epsilon_{F\_FCVI}$ had a similar effect on the diurnal trend of the data. Results from this study are limited to barley cultivars and should be confirmed by investigating structurally different plant types. In summary, both downscaling methods for scaling TOC $F_{760}$ to leaf $F_{760}$ were found to be effective, except for FCVI in sparse canopies, and are applicable to high spatial resolutions $F_{760}$ observations.

## Funding

AirSIF was supported by the Australian Research Council (ARC) [grant number DP140101488]. J.B. was supported by a Research Scholarship of the German Research Foundation (DFG) [grant number GZ: BE 5882/1–1]. Z.M. was supported by the Australian Research

Council Future Fellowship [grant number FT160100477]. We gratefully acknowledge the financial support by the European Space Agency (ESA) for airborne data acquisition and data analysis in the frame of the FLEXSense campaign [ESA Contract No. 4000125402/18/NL/NA] and the Photoproxy project [ESA contract No. 4000125731/19/NL/LF]. Additionally, this work has partially been funded by the German Federal Ministry of Education and Research within the German-Plant-Phenotyping Network (DPPN) [project identification number 031A053]. Open access fees were funded by the Deutsche Forschungsgemeinschaft (DFG, German Research Foundation) – 491111487.

## CRediT authorship contribution statement

**Juliane Bendig:** Writing – review & editing, Writing – original draft, Visualization, Methodology, Investigation, Funding acquisition, Formal analysis, Data curation, Conceptualization. **Zbyněk Malenovský:** Writing – review & editing, Writing – original draft, Validation, Methodology, Investigation, Funding acquisition, Conceptualization. **Bastian Siegmann:** Writing – review & editing, Investigation, Data curation, Conceptualization. **Julie Krämer:** Writing – review & editing, Investigation, Data curation. **Uwe Rascher:** Writing – review & editing, Supervision, Project administration.

## Declaration of competing interest

Authors declare no competing interest.

## Acknowledgement

We thank: Arko Lucieer, Darren Turner, Deepak Gautam, and Richard Ballard (University of Tasmania) for facilitating the use of AirSIF during the FLEXSense 2018 campaign, Lasse Klingbeil (Bonn University) for providing drone equipment, Moritz Prüm and Marcel Dogotari (Rhine-Waal University of Applied Sciences) for piloting the drone, Georg Bareth and his team for providing the RTK GNSS, Patrick Rademske, Verena Trinkel and the entire team at IBG-2 (Research Centre Jülich) for providing the HyPlant dataset and performing lab analysis of plant samples, the team at Field Lab Campus Klein-Altendorf (University of Bonn) for growing the experimental barley crops, Andre Krause and Lars Gruenhagen for their support during the field work, Sergio Cogliati (University Milano-Bicocca) for his support with SIF retrievals, and Jean Philippe Gastellu-Etchegorry (CESBIO Toulouse) for supporting our DART modelling.

## Appendix A

Settings and values of input parameters used for discrete anisotropic radiative transfer (DART) simulations of barley plots (PAR = photosynthetically active radiation, VIS = visible wavelengths, F = fluorescence). The most essential DART settings can be found in the main document (Table 3).

| Parameter | Unit | Value |
|---|---|---|
| ***3D scene*** | | |
| Voxel dimensions (fixed) | m | x = 0.5, y = 0.5, z = 0.5 |
| Horizontal & vertical dimensions (fixed) | m | x = 1, y = 1, z = 0.6 |
| Slope (fixed) | ° | 0 |
| Geolocation & elevation (fixed) | ° & m.a.s.l. | Lat. = 50° N, Long. = 7° E, Alt. = 225 |
| ***Spectral settings*** | | |
| Solar irradiance (varied) | $W{\cdot}m^{-2}{\cdot}nm^{-1}$ | Measured per wavelength with radiometrically calibrated drone based AirSIF spectroradiometer in diurnal cycle of 29 June 2018 |
| Ration of direct vs. diffuse irradiance – SKYL (varied) | rel. | Measured per wavelength with radiometrically calibrated PAR ceptometer in diurnal cycle 29/06/2022 |
| Soil reflectance (fixed) | % | Measured in-situ: 18 % at 550 nm, 26 % at 686 nm, 28 % at 740 nm |
| PAR spectral band (VIS) (fixed) | nm | 400–700 (centre at 550 nm) |
| Fluorescence spectral band (fixed) | nm | 759.6–760.4 (centre at 760 nm) |
| ***Radiative transfer settings*** (all fixed) | | |
| Light propagation mode | – | Forward flux-tracking & radiative budget (without atmosphere) |
| Propagation threshold | – | 1.0E-7 |
| Max. no. of iterations | – | 10 |
| Scene albedo exitance threshold | – | 0.001 |
| Max. no. of scenes crossed by a ray | – | 1000 |
| Smaller mesh size of irradiance source | m | 0.001 |
| Illumination spatial distribution | – | Semi-random |
| Factor N for division sub-cells per cell | – | 2 |
| Factor M for division sub-face per face | – | 4 |
| Barycentre on intercepted surfaces | – | yes |
| Barycentre on exiting sub-surfaces | – | yes |
| Use of sparse voxel acceleration | – | yes |
| No. of triangles for acceleration inside a voxel | – | 10 |

## Appendix B

Linear regressions of leaf and TOC nadir* $F_{760}$ simulated in DART for LAI 0.5–8 (shown in separate panels) and coloured according to LAD (i.e., erectophile, planophile, and spherical). The dashed line indicates the 1:1 line, the black line represents the combined linear regression for all three LADs and $R^2$ indicate the coefficient of determination for these regressions. Input values for the DART simulations are listed in Table 3. *Hemi-spherical-directional reflectance factor and oblique multidirectional $F_{760}$ were also simulated but are not shown here.

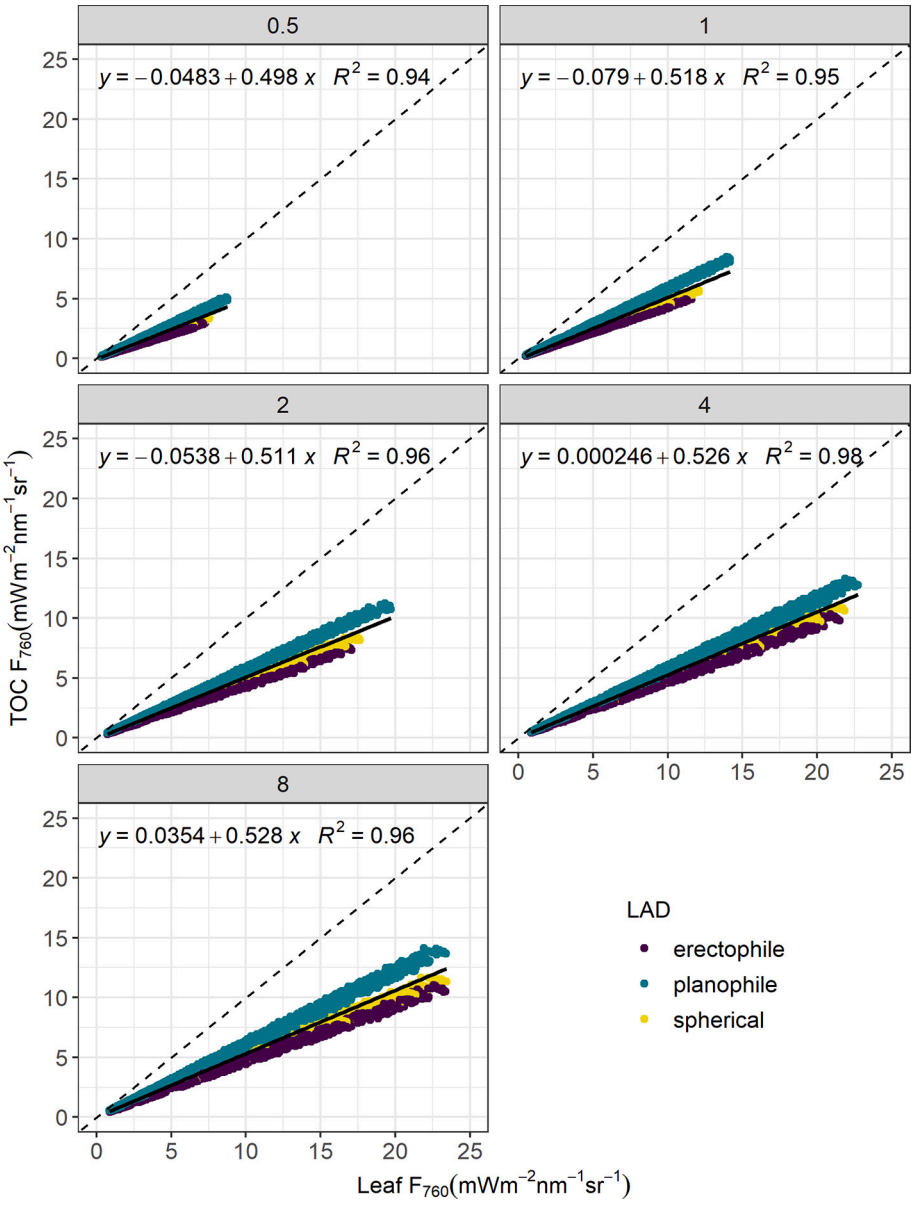

## Appendix C

Comparison of DART-simulated leaf level $F_{760}$ efficiency factor $\epsilon_{F\_leaf}$ against $\epsilon_{F\_FCVI}$ and $\epsilon_{F\_NIRvH1}$ for sensor viewing angels close to the hotspot per LAI between 0.5 and 8, coloured by the local time/SZA. The dashed line indicates the 1:1 line, the black line is the linear regression line for all displayed simulations together. $R^2$ indicates its coefficient of determination, RMSE stands for the root mean square error, and MAPE for mean absolute percent error. Input values for the DART simulation are listed in Table 3.

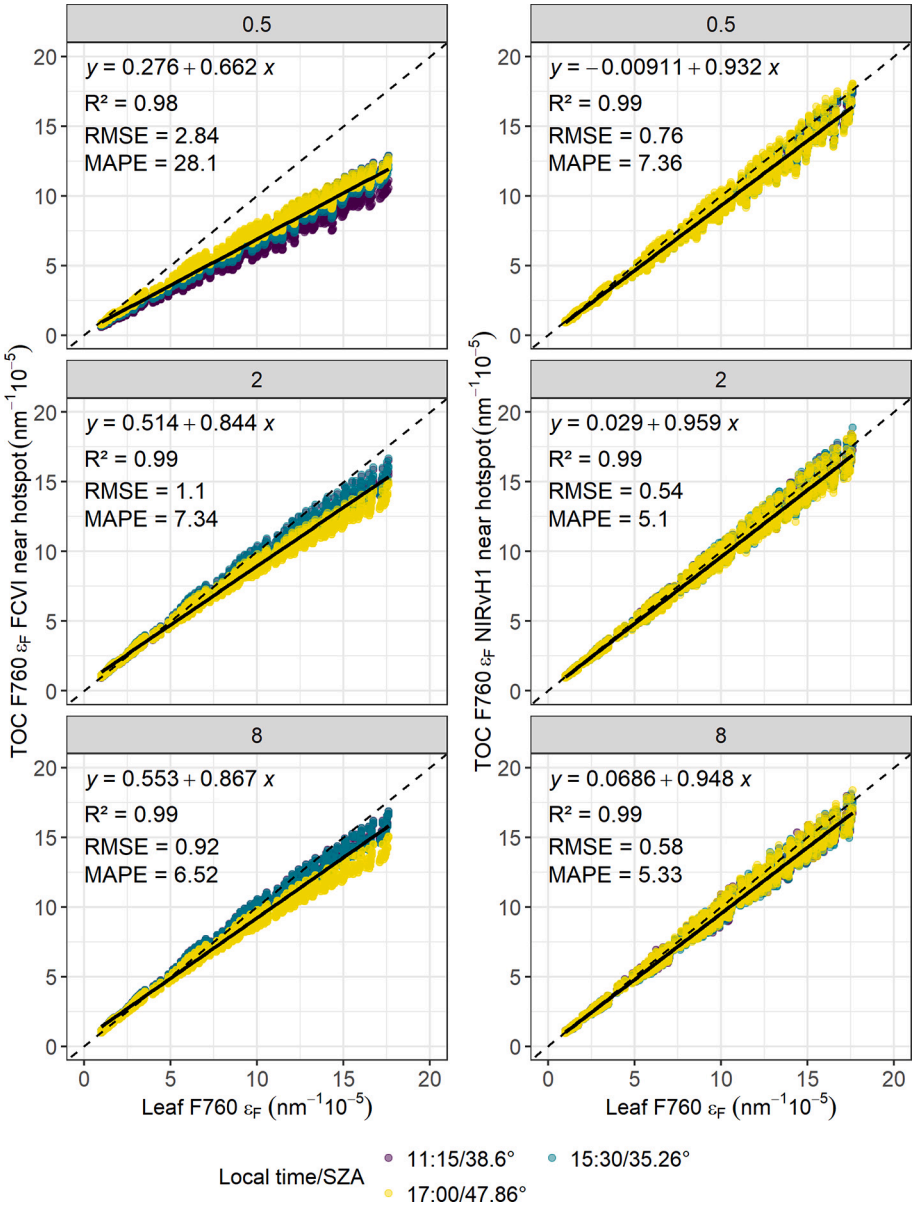

## Appendix D

Comparison of DART-simulated leaf level $F_{760}$ efficiency factor $\epsilon_{F\_leaf}$ against $\epsilon_{F\_FCVI}$ and $\epsilon_{F\_NIRvH1}$ for sensor viewing angles close to the darkspot (i.e., opposite to hotspot) for LAI between 0.5 and 8, coloured by the local time/SZA. The dashed line indicates the 1:1 line, the black line is the linear regression line for all displayed simulations together. $R^2$ indicates its coefficient of determination, RMSE stands for the root mean square error, and MAPE for mean absolute percent error. Input values for the DART simulation are listed in Table 3.

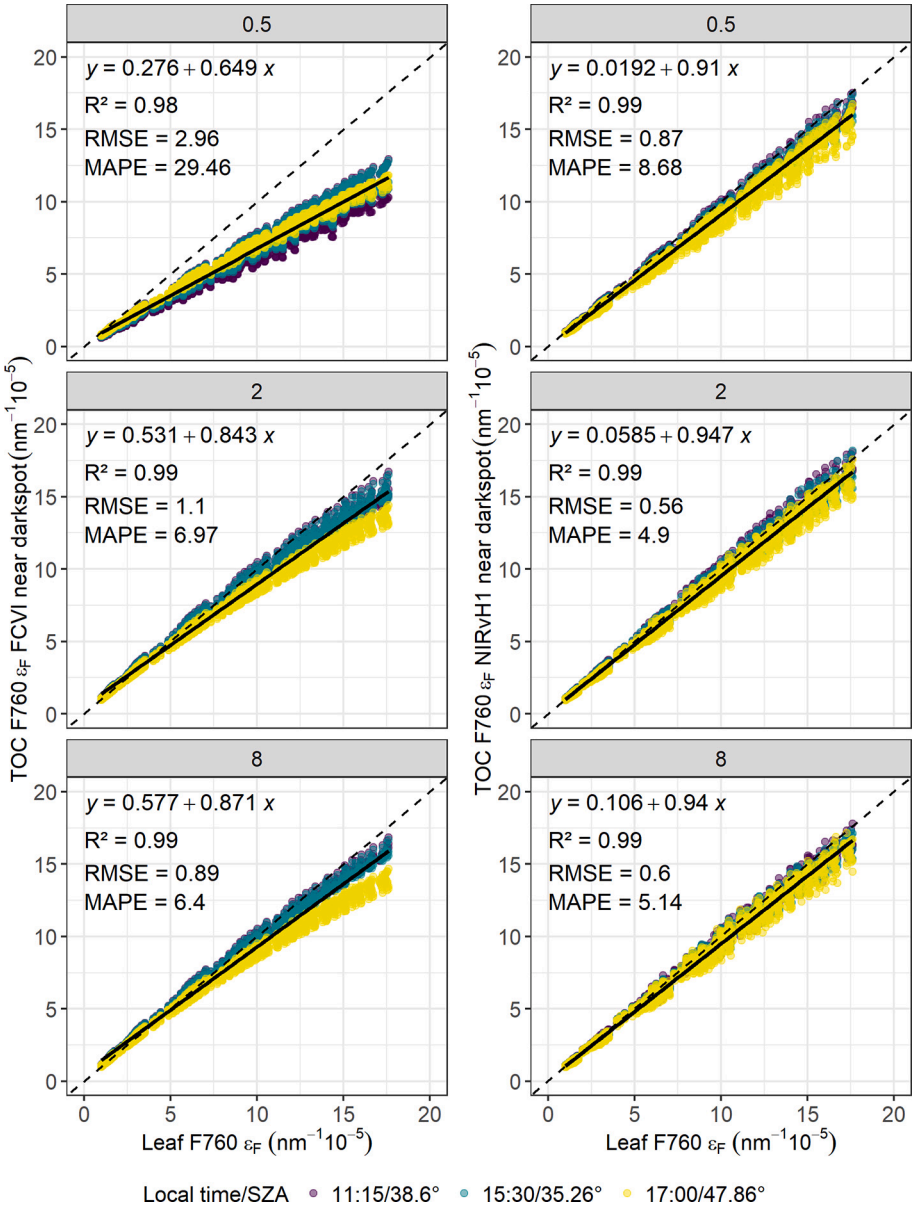


## Appendix E. Supplementary data

Supplementary data to this article can be found online at https://doi.org/10.1016/j.rse.2024.114521.

## Data availability

Data will be made available on request.

## References

Bendig, J., Chang, C.Y., Wang, N., Atherton, J., Malenovský, Z., Rascher, U., 2021. Measuring solar-induced fluorescence from unmanned aircraft systems for operational use in plant phenotyping and precision farming. In: 2021 IEEE International Geoscience and Remote Sensing Symposium IGARSS. Presented at the 2021 IEEE International Geoscience and Remote Sensing Symposium IGARSS, pp. 1921–1924. https://doi.org/10.1109/IGARSS47720.2021.9555157.

Bendig, J., Malenovský, Z., Gautam, D., Lucieer, A., 2019. Solar-induced chlorophyll fluorescence measured from an unmanned aircraft system: sensor etaloning and platform motion correction. IEEE Trans. Geosci. Remote Sens. 58, 3437–3444. https://doi.org/10.1109/TGRS.2019.2956194.

Berger, K., Atzberger, C., Danner, M., D'Urso, G., Mauser, W., Vuolo, F., Hank, T., 2018. Evaluation of the PROSAIL model capabilities for future hyperspectral model environments: a review study. Remote Sens. 10, 85. https://doi.org/10.3390/rs10010085.

Berk, A., Anderson, G.P., Acharya, P.K., Bernstein, L.S., Muratov, L., Lee, J., Fox, M.J., Adler-Golden, S.M., Chetwynd, J.H., Hoke, M.L., Lockwood, R.B., Cooley, T.W., Gardner, J.A., 2005. MODTRAN5: a reformulated atmospheric band model with auxiliary species and practical multiple scattering options. In: Multispectral and Hyperspectral Remote Sensing Instruments and Applications II. Presented at the Multispectral and Hyperspectral Remote Sensing Instruments and Applications II. International Society for Optics and Photonics, pp. 88–95. https://doi.org/10.1117/12.578758.

Biriukova, K., Celesti, M., Evdokimov, A., Pacheco-Labrador, J., Julitta, T., Migliavacca, M., Giardino, C., Miglietta, F., Colombo, R., Panigada, C., Rossini, M., 2020. Effects of varying solar-view geometry and canopy structure on solar-induced chlorophyll fluorescence and PRI. Int. J. Appl. Earth Obs. Geoinf. 89, 102069. https://doi.org/10.1016/j.jag.2020.102069.

Campbell, P.K.E., Huemmrich, K.F., Middleton, E.M., Ward, L.A., Julitta, T., Daughtry, C. S.T., Burkart, A., Russ, A.L., Kustas, W.P., 2019. Diurnal and seasonal variations in chlorophyll fluorescence associated with photosynthesis at leaf and canopy scales. Remote Sens. 11, 488. https://doi.org/10.3390/rs11050488.

Chang, C.Y., Zhou, R., Kira, O., Marri, S., Skovira, J., Gu, L., Sun, Y., 2020. An unmanned aerial system (UAS) for concurrent measurements of solar-induced chlorophyll fluorescence and hyperspectral reflectance toward improving crop monitoring. Agric. For. Meteorol. 294, 108145. https://doi.org/10.1016/j.agrformet.2020.108145.

Cogliati, S., Verhoef, W., Kraft, S., Sabater, N., Alonso, L., Vicent, J., Moreno, J., Drusch, M., Colombo, R., 2015. Retrieval of sun-induced fluorescence using advanced spectral fitting methods. Remote Sens. Environ. 169, 344–357. https://doi.org/10.1016/j.rse.2015.08.022.

Dechant, B., Ryu, Y., Badgley, G., Köhler, P., Rascher, U., Migliavacca, M., Zhang, Y., Tagliabue, G., Guan, K., Rossini, M., Goulas, Y., Zeng, Y., Frankenberg, C., Berry, J. A., 2022. NIRVP: a robust structural proxy for sun-induced chlorophyll fluorescence and photosynthesis across scales. Remote Sens. Environ. 268, 112763. https://doi.org/10.1016/j.rse.2021.112763.

Féret, J.-B., Gitelson, A.A., Noble, S.D., Jacquemoud, S., 2017. PROSPECT-D: towards modeling leaf optical properties through a complete lifecycle. Remote Sens. Environ. 193, 204–215. https://doi.org/10.1016/j.rse.2017.03.004.

Féret, J.-B., Berger, K., de Boissieu, F., Malenovský, Z., 2021. PROSPECT-PRO for estimating content of nitrogen-containing leaf proteins and other carbon-based constituents. Remote Sens. Environ. 252, 112173. https://doi.org/10.1016/j.rse.2020.112173.

Fournier, A., Daumard, F., Champagne, S., Ounis, A., Goulas, Y., Moya, I., 2012. Effect of canopy structure on sun-induced chlorophyll fluorescence. ISPRS J. Photogramm. Remote Sens. 68, 112–120. https://doi.org/10.1016/j.isprsjprs.2012.01.003.

Garcia Millan, V.E., Rankine, C., Sanchez-Azofeifa, G.A., 2020. Crop loss evaluation using digital surface models from unmanned aerial vehicles data. Remote Sens. 12, 981. https://doi.org/10.3390/rs12060981.

Gastellu-Etchegorry, J., Lauret, N., Yin, T., Landier, L., Kallel, A., Malenovský, Z., Bitar, A.A., Aval, J., Benhmida, S., Qi, J., Medjdoub, G., Guilleux, J., Chavanon, E., Cook, B., Morton, D., Chrysoulakis, N., Mitraka, Z., 2017. DART: recent advances in remote sensing data modeling with atmosphere, polarization, and chlorophyll fluorescence. IEEE J. Sel. Top. Appl. Earth Obs. Remote Sens. 10, 2640–2649. https://doi.org/10.1109/JSTARS.2017.2685528.

Gautam, D., Lucieer, A., Bendig, J., Malenovský, Z., 2020. Footprint determination of a spectroradiometer mounted on an unmanned aircraft system. IEEE Trans. Geosci. Remote Sens. 58, 3085–3096. https://doi.org/10.1109/TGRS.2019.2947703.

Guanter, L., Zhang, Y., Jung, M., Joiner, J., Voigt, M., Berry, J.A., Frankenberg, C., Huete, A.R., Zarco-Tejada, P., Lee, J.-E., Moran, M.S., Ponce-Campos, G., Beer, C., Camps-Valls, G., Buchmann, N., Gianelle, D., Klumpp, K., Cescatti, A., Baker, J.M., Griffis, T.J., 2014. Global and time-resolved monitoring of crop photosynthesis with chlorophyll fluorescence. Proc. Natl. Acad. Sci. 111, E1327–E1333. https://doi.org/10.1073/pnas.1320008111.

Hampel, F.R., 1974. The influence curve and its role in robust estimation. J. Am. Stat. Assoc. 69, 383–393. https://doi.org/10.1080/01621459.1974.10482962.

Hao, D., Asrar, G.R., Zeng, Y., Yang, X., Li, X., Xiao, J., Guan, K., Wen, J., Xiao, Q., Berry, J.A., Chen, M., 2021. Potential of hotspot solar-induced chlorophyll fluorescence for better tracking terrestrial photosynthesis. Glob. Chang. Biol. 27, 2144–2158. https://doi.org/10.1111/gcb.15554.

Imbery, F., Friedrich, K., Haeseler, S., Koppe, C., Janssen, W., Bissolli, P., 2018. Vorläufiger Rückblick auf den Sommer 2018 – eine Bilanz extremer Wetterereignisse. Rep. Ger. Weather Serv. Dtsch, Wetterd. https://www.dwd.de/DE/leistungen/besondereereignisse/temperatur/20180803_bericht_sommer2018.pdf?_blob=publicationFile&v=10 (accessed 11 October 2024).

Jacquemoud, S., Ustin, S.L., Verdebout, J., Schmuck, G., Andreoli, G., Hosgood, B., 1996. Estimating leaf biochemistry using the PROSPECT leaf optical properties model. Remote Sens. Environ. 56, 194–202. https://doi.org/10.1016/0034-4257(95)00238-3.

Jacquemoud, S., Verhoef, W., Baret, F., Bacour, C., Zarco-Tejada, P.J., Asner, G.P., François, C., Ustin, S.L., 2009. PROSPECT+SAIL models: a review of use for vegetation characterization. Remote Sens. Environ. 113, S56–S66. https://doi.org/10.1016/j.rse.2008.01.026.

Knyazikhin, Y., Schull, M.A., Stenberg, P., Mõttus, M., Rautiainen, M., Yang, Y., Marshak, A., Carmona, P.L., Kaufmann, R.K., Lewis, P., Disney, M.I., Vanderbilt, V., Davis, A.B., Baret, F., Jacquemoud, S., Lyapustin, A., Myneni, R.B., 2013. Hyperspectral remote sensing of foliar nitrogen content. Proc. Natl. Acad. Sci. 110, E185–E192. https://doi.org/10.1073/pnas.1210196109.

Krämer, J., Siegmann, B., Kraska, T., Muller, O., Rascher, U., 2021. The potential of spatial aggregation to extract remotely sensed sun-induced fluorescence (SIF) of small-sized experimental plots for applications in crop phenotyping. Int. J. Appl. Earth Obs. Geoinf. 104, 102565. https://doi.org/10.1016/j.jag.2021.102565.

Lamsal, K., Malenovský, Z., Woodgate, W., Waterman, M., Brodribb, T.J., Aryal, J., 2022. Spectral retrieval of eucalypt leaf biochemical traits by inversion of the Fluspect-Cx model. Remote Sens. 14, 567. https://doi.org/10.3390/rs14030567.

Liu, X., Guanter, L., Liu, L., Damm, A., Malenovský, Z., Rascher, U., Peng, D., Du, S., Gastellu-Etchegorry, J.-P., 2019. Downscaling of solar-induced chlorophyll fluorescence from canopy level to photosystem level using a random forest model. Remote Sens. Environ. https://doi.org/10.1016/j.rse.2018.05.035.

Lucieer, A., Malenovský, Z., Veness, T., Wallace, L., 2014. HyperUAS-imaging spectroscopy from a multirotor unmanned aircraft system: HyperUAS-imaging spectroscopy from a multirotor unmanned. J. Field Robot. 31, 571–590. https://doi.org/10.1002/rob.21508.

Mac Arthur, A., MacLellan, C.J., Malthus, T., 2012. The fields of view and directional response functions of two field Spectroradiometers. IEEE Trans. Geosci. Remote Sens. 50, 3892–3907. https://doi.org/10.1109/TGRS.2012.2185055.

Malenovský, Z., Regaieg, O., Yin, T., Lauret, N., Guilleux, J., Chavanon, E., Duran, N., Janoutová, R., Delavois, A., Meynier, J., Medjdoub, G., Yang, P., van der Tol, C., Morton, D., Cook, B.D., Gastellu-Etchegorry, J.-P., 2021. Discrete anisotropic radiative transfer modelling of solar-induced chlorophyll fluorescence: structural impacts in geometrically explicit vegetation canopies. Remote Sens. Environ. 263, 112564. https://doi.org/10.1016/j.rse.2021.112564.

Mancini, F., Dubbini, M., Gattelli, M., Stecchi, F., Fabbri, S., Gabbianelli, G., 2013. Using unmanned aerial vehicles (UAV) for high-resolution reconstruction of topography: the structure from motion approach on coastal environments. Remote Sens. 5, 6880–6898. https://doi.org/10.3390/rs5126880.

Meroni, M., Colombo, R., 2006. Leaf level detection of solar induced chlorophyll fluorescence by means of a subnanometer resolution spectroradiometer. Remote Sens. Environ. 103, 438–448. https://doi.org/10.1016/j.rse.2006.03.016.

Meroni, M., Busetto, L., Colombo, R., Guanter, L., Moreno, J., Verhoef, W., 2010. Performance of spectral fitting methods for vegetation fluorescence quantification. Remote Sens. Environ. 114, 363–374. https://doi.org/10.1016/j.rse.2009.09.010.

Merrick, T., Pau, S., Detto, M., Broadbent, E.N., Bohlman, S.A., Still, C.J., Almeyda Zambrano, A.M., 2021. Unveiling spatial and temporal heterogeneity of a tropical forest canopy using high-resolution NIRv, FCVI, and NIRvrad from UAS observations. Biogeosciences 18, 6077–6091. https://doi.org/10.5194/bg-18-6077-2021.

Mohammed, G.H., Colombo, R., Middleton, E.M., Rascher, U., van der Tol, C., Nedbal, L., Goulas, Y., Pérez-Priego, O., Damm, A., Meroni, M., Joiner, J., Cogliati, S., Verhoef, W., Malenovský, Z., Gastellu-Etchegorry, J.-P., Miller, J.R., Guanter, L., Moreno, J., Moya, I., Berry, J.A., Frankenberg, C., Zarco-Tejada, P.J., 2019. Remote sensing of solar-induced chlorophyll fluorescence (SIF) in vegetation: 50 years of progress. Remote Sens. Environ. 231, 111177. https://doi.org/10.1016/j.rse.2019.04.030.

Monteith, J.L., 1977. Climate and the efficiency of crop production in Britain. Philos. Trans. R. Soc. Lond. B Biol. Sci. 281, 277–294.

Nagy, Z., Balogh, J., Petrás, D., Fóti, S., MacArthur, A., Pintér, K., 2024. Detecting drought stress occurrence using synergies between Sun induced fluorescence and vegetation surface temperature spatial records. Sci. Total Environ. 907, 168053. https://doi.org/10.1016/j.scitotenv.2023.168053.

Otsu, N., 1979. A threshold selection method from gray-level histograms. IEEE Trans. Syst. Man Cybern. SMC-9, 62–66.

Porcar-Castell, A., Malenovský, Z., Magney, T., Van Wittenberghe, S., Fernández-Marín, B., Maignan, F., Zhang, Y., Maseyk, K., Atherton, J., Albert, L.P., Robson, T. M., Zhao, F., Garcia-Plazaola, J.-I., Ensminger, I., Rajewicz, P.A., Grebe, S., Tikkanen, M., Kellner, J.R., Ihalainen, J.A., Rascher, U., Logan, B., 2021. Chlorophyll a fluorescence illuminates a path connecting plant molecular biology to Earth-system science. Nat. Plants 1–12. https://doi.org/10.1038/s41477-021-00980-4.

R Core Team, 2021. R: A language and environment for statistical computing. R Foundation for Statistical Computing, Vienna, Austria. URL. https://www.R-project.org/.

Rascher, U., Alonso, L., Burkart, A., Cilia, C., Cogliati, S., Colombo, R., Damm, A., Drusch, M., Guanter, L., Hanus, J., Hyvärinen, T., Julitta, T., Jussila, J., Kataja, K., Kokkalis, P., Kraft, S., Kraska, T., Matveeva, M., Moreno, J., Muller, O., Panigada, C., Pikl, M., Pinto, F., Prey, L., Pude, R., Rossini, M., Schickling, A., Schurr, U., Schüttemeyer, D., Verrelst, J., Zemek, F., 2015. Sun-induced fluorescence – a new probe of photosynthesis: first maps from the imaging spectrometer HyPlant. Glob. Chang. Biol. 21, 4673–4684. https://doi.org/10.1111/gcb.13017.

Rascher, U., Baum, S., Siegmann, B., Buffat, J., Burkart, A., Cogliati, S., Herrera, D., Julitta, T., Knopf, O., Miglietta, F., Muller, O., Vargas, J.Q., 2022. FLEXSense: Technical Assistance for Airborne Measurements during the FLEX Sentinel Tandem Experiment (Final Report FLEXSense CCN1 No. ESA Contract No. 4000125402/18/NL/NA).

Regaieg, O., Yin, T., Malenovský, Z., Cook, B.D., Morton, D.C., Gastellu-Etchegorry, J.-P., 2021. Assessing impacts of canopy 3D structure on chlorophyll fluorescence radiance and radiative budget of deciduous forest stands using DART. Remote Sens. Environ. 265, 112673. https://doi.org/10.1016/j.rse.2021.112673.

Siegmann, B., Alonso, L., Celesti, M., Cogliati, S., Colombo, R., Damm, A., Douglas, S., Guanter, L., Hanuš, J., Kataja, K., Kraska, T., Matveeva, M., Moreno, J., Muller, O., Pikl, M., Pinto, F., Quirós Vargas, J., Rademske, P., Rodriguez-Morene, F., Sabater, N., Schickling, A., Schüttemeyer, D., Zemek, F., Rascher, U., 2019. The high-performance airborne imaging spectrometer HyPlant—from raw images to top-of-

canopy reflectance and fluorescence products: introduction of an automatized processing chain. Remote Sens. 11, 2760. https://doi.org/10.3390/rs11232760.
Siegmann, B., Cendrero-Mateo, M.P., Cogliati, S., Damm, A., Gamon, J., Herrera, D., Jedmowski, C., Junker-Frohn, L.V., Kraska, T., Muller, O., Rademske, P., van der Tol, C., Quiros-Vargas, J., Yang, P., Rascher, U., 2021. Downscaling of far-red solar-induced chlorophyll fluorescence of different crops from canopy to leaf level using a diurnal data set acquired by the airborne imaging spectrometer HyPlant. Remote Sens. Environ. 264, 112609. https://doi.org/10.1016/j.rse.2021.112609.
Vargas, J.Q., Bendig, J., Mac Arthur, A., Burkart, A., Julitta, T., Maseyk, K., Thomas, R., Siegmann, B., Rossini, M., Celesti, M., Schüttemeyer, D., Kraska, T., Muller, O., Rascher, U., 2020. Unmanned aerial systems (UAS)-based methods for solar induced chlorophyll fluorescence (SIF) retrieval with non-imaging spectrometers: state of the art. Remote Sens. 12, 1624. https://doi.org/10.3390/rs12101624.
Verrelst, J., Rivera, J.P., Leonenko, G., Alonso, L., Moreno, J., 2014. Optimizing LUT-based RTM inversion for semiautomatic mapping of crop biophysical parameters from Sentinel-2 and -3 data: role of cost functions. IEEE Trans. Geosci. Remote Sens. 52, 257–269. https://doi.org/10.1109/TGRS.2013.2238242.
Vilfan, N., Van der Tol, C., Yang, P., Wyber, R., Malenovský, Z., Robinson, S.A., Verhoef, W., 2018. Extending Fluspect to simulate xanthophyll driven leaf reflectance dynamics. Remote Sens. Environ. 211, 345–356. https://doi.org/10.1016/j.rse.2018.04.012.
Wang, N., Suomalainen, J., Bartholomeus, H., Kooistra, L., Masiliūnas, D., Clevers, J.G.P.W., 2021. Diurnal variation of sun-induced chlorophyll fluorescence of agricultural crops observed from a point-based spectrometer on a UAV. Int. J. Appl. Earth Obs. Geoinf. 96, 102276. https://doi.org/10.1016/j.jag.2020.102276.
Wang, N., Siegmann, B., Rascher, U., Clevers, J.G.P.W., Muller, O., Bartholomeus, H., Bendig, J., Masiliūnas, D., Pude, R., Kooistra, L., 2022. Comparison of a UAV- and an airborne-based system to acquire far-red sun-induced chlorophyll fluorescence measurements over structurally different crops. Agric. For. Meteorol. 323, 109081. https://doi.org/10.1016/j.agrformet.2022.109081.
Wieneke, S., Ahrends, H., Damm, A., Pinto, F., Stadler, A., Rossini, M., Rascher, U., 2016. Airborne based spectroscopy of red and far-red sun-induced chlorophyll fluorescence: implications for improved estimates of gross primary productivity. Remote Sens. Environ. 184, 654–667. https://doi.org/10.1016/j.rse.2016.07.025.
Wu, G., Guan, K., Ainsworth, E.A., Martin, D.G., Kimm, H., Yang, X., 2023. Solar-induced chlorophyll fluorescence captures the effects of elevated ozone on canopy structure and acceleration of senescence in soybean. J. Exp. Bot. erad356. https://doi.org/10.1093/jxb/erad356.
Xu, S., Atherton, J., Riikonen, A., Zhang, C., Oivukkamäki, J., MacArthur, A., Honkavaara, E., Hakala, T., Koivumäki, N., Liu, Z., Porcar-Castell, A., 2021. Structural and photosynthetic dynamics mediate the response of SIF to water stress in a potato crop. Remote Sens. Environ. 263, 112555. https://doi.org/10.1016/j.rse.2021.112555.
Yang, P., van der Tol, C., 2018. Linking canopy scattering of far-red sun-induced chlorophyll fluorescence with reflectance. Remote Sens. Environ. 209, 456–467. https://doi.org/10.1016/j.rse.2018.02.029.
Yang, P., van der Tol, C., Verhoef, W., Damm, A., Schickling, A., Kraska, T., Muller, O., Rascher, U., 2019. Using reflectance to explain vegetation biochemical and structural effects on sun-induced chlorophyll fluorescence. Remote Sens. Environ. 231, 110996. https://doi.org/10.1016/j.rse.2018.11.039.
Yang, P., van der Tol, C., Campbell, P.K.E., Middleton, E.M., 2020. Fluorescence correction vegetation index (FCVI): a physically based reflectance index to separate physiological and non-physiological information in far-red sun-induced chlorophyll fluorescence. Remote Sens. Environ. 240, 111676. https://doi.org/10.1016/j.rse.2020.111676.
Yang, P., Prikaziuk, E., Verhoef, W., van der Tol, C., 2021a. SCOPE 2.0: a model to simulate vegetated land surface fluxes and satellite signals. Geosci. Model Dev. 14, 4697–4712. https://doi.org/10.5194/gmd-14-4697-2021.
Yang, P., Van Der Tol, C., Campbell, P.K.E., Middleton, E.M., 2021b. Unraveling the physical and physiological basis for the solar- induced chlorophyll fluorescence and photosynthesis relationship using continuous leaf and canopy measurements of a corn crop. Biogeosciences 18, 441–465. https://doi.org/10.5194/bg-18-441-2021.
Yang, P., Liu, X., Liu, Z., van der Tol, C., Liu, L., 2023. The roles of radiative, structural and physiological information of sun-induced chlorophyll fluorescence in predicting gross primary production of a corn crop at various temporal scales. Agric. For. Meteorol. 342, 109720. https://doi.org/10.1016/j.agrformet.2023.109720.
Zarco-Tejada, P.J., González-Dugo, M.V., Fereres, E., 2016. Seasonal stability of chlorophyll fluorescence quantified from airborne hyperspectral imagery as an indicator of net photosynthesis in the context of precision agriculture. Remote Sens. Environ. 179, 89–103. https://doi.org/10.1016/j.rse.2016.03.024.
Zeng, Y., Badgley, G., Dechant, B., Ryu, Y., Chen, M., Berry, J.A., 2019. A practical approach for estimating the escape ratio of near-infrared solar-induced chlorophyll fluorescence. Remote Sens. Environ. 232, 111209. https://doi.org/10.1016/j.rse.2019.05.028.
Zeng, Y., Hao, D., Badgley, G., Damm, A., Rascher, U., Ryu, Y., Johnson, J., Krieger, V., Wu, S., Qiu, H., Liu, Y., Berry, J.A., Chen, M., 2021. Estimating near-infrared reflectance of vegetation from hyperspectral data. Remote Sens. Environ. 267, 112723. https://doi.org/10.1016/j.rse.2021.112723.
Zhang, Y., Guanter, L., Berry, J.A., van der Tol, C., Yang, X., Tang, J., Zhang, F., 2016. Model-based analysis of the relationship between sun-induced chlorophyll fluorescence and gross primary production for remote sensing applications. Remote Sens. Environ. 187, 145–155. https://doi.org/10.1016/j.rse.2016.10.016.
Zhang, Z., Zhang, Y., Zhang, Q., Chen, J.M., Porcar-Castell, A., Guanter, L., Wu, Y., Zhang, X., Wang, H., Ding, D., Li, Z., 2020. Assessing bi-directional effects on the diurnal cycle of measured solar-induced chlorophyll fluorescence in crop canopies. Agric. For. Meteorol. 295, 108147. https://doi.org/10.1016/j.agrformet.2020.108147.
Zhang, Z., Zhang, X., Porcar-Castell, A., Chen, J.M., Ju, W., Wu, L., Wu, Y., Zhang, Y., 2022. Sun-induced chlorophyll fluorescence is more strongly related to photosynthesis with hemispherical than nadir measurements: evidence from field observations and model simulations. Remote Sens. Environ. 279, 113118. https://doi.org/10.1016/j.rse.2022.113118.